

How good nnU-Net for Segmenting Cardiac MRI: A Comprehensive Evaluation

Malitha Gunawardhana^{1*}, Fangqiang Xu¹ and Jichao Zhao¹

^{1*}Auckland Bioengineering Institute, University of Auckland, Auckland,
1010, New Zealand.

*Corresponding author(s). E-mail(s):
malithagunawardhana96@gmail.com;

Abstract

Background

Cardiac segmentation is a critical process in medical imaging, providing a detailed analysis of heart structures that is essential for the diagnosis and treatment of various cardiovascular diseases. The advent of deep learning has revolutionized this field by introducing automated segmentation techniques that significantly outperform traditional manual methods in terms of both accuracy and efficiency. The nnU-Net framework, in particular, has emerged as a highly robust and versatile tool for medical image segmentation, capable of adapting to a wide range of imaging modalities and segmentation tasks.

Methods

In this study, we systematically evaluate the performance of nnU-Net in segmenting cardiac magnetic resonance images (MRIs) using five distinct datasets: LAScarQs 2022, LASC 2018, ACDC, MnM1, and MnM2. We investigate the efficacy of various nnU-Net configurations, including 2D, 3D full resolution, 3D low resolution, 3D cascade, and ensemble models. Each configuration is assessed based on its ability to accurately delineate cardiac structures, with a focus on comparing their strengths and weaknesses across different cardiac segmentation tasks. The study employs a comprehensive benchmarking approach to evaluate the models' capabilities and identify potential areas for improvement.

Results

Our findings indicate that the nnU-Net configurations deliver state-of-the-art performance across all the datasets examined. Notably, the 2D configuration outperformed the 3D configuration in certain scenarios, demonstrating superior accuracy and efficiency. In some cases, the 2D model even surpassed other advanced approaches. However, ensemble methods did not consistently provide

additional benefits, highlighting that more complex models are not always superior. The analysis also reveals specific limitations in existing models, particularly in handling challenging segmentation tasks, underscoring the need for further refinement.

Conclusions

This study highlights the robustness and flexibility of nnU-Net configurations in cardiac MRI segmentation, affirming their effectiveness. However, the results also emphasize the need for developing new, specialized models to address particular segmentation challenges. These insights are valuable for guiding future research aimed at improving deep learning methodologies for more precise and efficient cardiac imaging analysis.

Keywords: MRI, Segmentation, nnU-Net, Benchmark

1 Introduction

Cardiovascular diseases (CVDs) accounted for an estimated 19.05 million deaths globally in 2020, reflecting an 18.71% increase from 2010. Despite this rise, the age-standardized death rate decreased by 12.19%, reaching 239.80 per 100,000 population. Additionally, the total crude prevalence of CVD worldwide reached 607.64 million cases in 2020, marking a 29.01% increase compared to 2010 [1]. These statistics underscore the urgent need for advanced diagnostic and therapeutic approaches in cardiology.

Accurate segmentation of cardiac structures is essential for understanding heart function, planning interventions, and monitoring disease progression. For example, locating and quantifying fibrosis and scars have been demonstrated to be valuable tools for the treatment stratification of patients with atrial fibrillation (AF) [2–4] and ventricular tachycardia [5]. These techniques provide critical guidance for surgical or ablation procedures [6], and imaging of post-ablation scars offers valuable insights into treatment outcomes [7].

Cardiac segmentation involves the precise delineation of key anatomical structures within the heart, including the myocardium, ventricles, atria, and major vessels. In particular, Late Gadolinium Enhancement Magnetic Resonance Imaging (LGE-MRI) has emerged as an invaluable technique in cardiac imaging. LGE-MRI excels in highlighting areas of myocardial scarring and fibrosis, which are critical indicators in the diagnosis and management of various cardiac conditions, including myocardial infarction, cardiomyopathy, and arrhythmia [8, 9].

Historically, manual segmentation by expert radiologists and cardiologists has been considered the gold standard for cardiac image analysis. However, this method is hindered by significant limitations, particularly its time-consuming nature, often requiring hours for a single dataset, making it impractical for busy clinical settings [10]. The advent of automated segmentation methods, especially those utilizing deep learning techniques, has transformed the field of cardiac imaging analysis. These methods offer substantial advantages over traditional manual approaches, including consistency and reproducibility by eliminating inter-observer variability, rapid analysis with deep learning models capable of segmenting cardiac structures within seconds, scalability for

application to large datasets, and the potential for continuous improvement as models can be fine-tuned and updated with increasing data availability.

Over the past decade, numerous approaches have been developed for automated cardiac segmentation, each with its own strengths and limitations. These methods have explored various approaches to improve segmentation accuracy and robustness, including utilizing uncertainty [11, 12], semi-supervised learning [13, 14], curriculum learning [15], and multi-task learning [16].

Despite these advancements, there remains a notable gap in the literature regarding the comprehensive evaluation of one particular architecture that has shown remarkable success in medical image segmentation across various domains: the nnU-Net (no-new-Net) [17]. The nnU-Net is a self-configuring method based on the U-Net architecture that automatically adapts preprocessing, network architecture, training, and post-processing to the specifics of a given dataset. While nnU-Net has demonstrated state-of-the-art performance in numerous biomedical segmentation challenges [18], its potential in the specific context of cardiac segmentation has not been thoroughly explored. This presents a significant research opportunity, as cardiac MRI poses unique challenges due to its high contrast between normal and scarred myocardium, potential artefacts, and variability in image quality across different scanners and institutions.

In this study, we aim to bridge this knowledge gap by conducting a comprehensive analysis of nnU-Net’s performance in segmenting cardiac MRI. We utilize five widely used datasets for this task. Those are LAScarQS 2022 dataset [19], 2018 LASC dataset [20], ACDC dataset [21], MnM [22] and MnM2 datasets [23]. To the best of our knowledge, this is the first study to focus exclusively on this combination of methodology and imaging modality. By conducting this comprehensive analysis, we aim to provide the medical imaging community with valuable insights into the capabilities and limitations of nnU-Net for segmenting cardiac MRI. Our findings could potentially influence future directions in algorithm development, clinical adoption of automated segmentation tools, and standardization efforts in cardiac imaging analysis.

2 Method

2.1 nnU-Net architecture

The nnU-Net framework is specifically designed for semantic segmentation and is capable of handling both 2D and 3D images with various input modalities or channels. It adeptly processes voxel spacing and anisotropies and exhibits robustness even in scenarios where class distributions are highly imbalanced. Utilizing supervised learning, nnU-Net necessitates the provision of annotated training cases tailored to the application at hand. The quantity of required training cases can vary significantly depending on the complexity of the segmentation task, though nnU-Net often requires fewer cases than other solutions due to its extensive data augmentation strategies.

A key expectation for nnU-Net is its ability to process entire images during both the preprocessing and post-processing stages, making it unsuitable for exceedingly large images. Nevertheless, it has been successfully tested on images ranging from 40x40x40 pixels up to 1500x1500x1500 in 3D and from 40x40 up to approximately 30000x30000 in 2D. The capacity for handling larger images is contingent on the available RAM.

When presented with a new dataset, nnU-Net systematically analyzes the provided training cases to generate a 'dataset fingerprint'. Based on this analysis, it constructs several U-Net configurations tailored to the dataset:

- 2D U-Net :- Applicable for both 2D and 3D datasets.
- 3D Full Resolution U-Net :- Operates on high-resolution images and is intended for 3D datasets
- 3D Low Resolution U-Net :- Operates on low-resolution images
- 3D Cascade Full Resolution U-Net:- A 3D U-Net cascade where an initial low-resolution 3D U-Net refines predictions through a subsequent high-resolution 3D U-Net. This configuration is applied to large 3D datasets.

For datasets with smaller image sizes, the U-Net cascade (and thus the 3D low-resolution configuration) is excluded, as the patch size of the full-resolution U-Net is sufficient to cover a significant portion of the input images. The configuration of nnU-Net's segmentation pipelines is based on a three-step approach:

- Fixed Parameters: These parameters remain constant and are not adapted. Through the development of nnU-Net, a robust configuration was identified that includes the loss function, most data augmentation strategies, and the learning rate.
- Rule-Based Parameters: These parameters are adjusted based on the dataset fingerprint using heuristic rules. For instance, network topology, which includes pooling behaviour and network depth, is adapted to the patch size. The patch size, network topology, and batch size are optimized jointly, considering GPU memory constraints.
- Empirical Parameters: These parameters are determined through trial and error. This involves selecting the most suitable U-Net configuration for the dataset (2D, 3D full resolution, 3D low resolution, 3D cascade) and optimizing the postprocessing strategy.

nnU-Net's systematic approach to configuring segmentation pipelines based on dataset-specific characteristics and robust default settings makes it a versatile and powerful tool for semantic segmentation tasks.

2.2 Datasets

In this study, we utilized five datasets. Those are namely Left atrial and Scar Quantification and segmentation Challenge (LAScarQS) 2022 dataset [19], 2018 Atria Segmentation Challenge (LASC) [20], Automated Cardiac Diagnosis Challenge (ACDC)-2017 [21], Multi-Centre, Multi-Vendor and Multi-Disease Cardiac Image Segmentation Challenge (MnM) [22] and MnM2 [23].

2.2.1 LAScarQS Challenge Dataset

The LAScarQS challenge encompasses two primary tasks. The first task involves segmenting the left atrium (LA) cavity and scars, while the second task focuses solely on segmenting the LA cavity. For Task 1, the dataset includes 60 training images with corresponding labels and 10 validation images without labels. Task 2 provides 130 training images with labels and 20 validation images without labels. Consequently,

only the training data can be utilized for both training and testing purposes. For Task 1, we allocated 50 images for training and the remaining 10 for testing. For Task 2, we used 115 images for training and 15 for testing.

The LGE-MRIs in this challenge were sourced from the University of Utah, Beth Israel Deaconess Medical Center, and King’s College London. The scans were performed using Siemens Avanto 1.5 T, Siemens Vario 3 T, or Philips Acheiva 1.5 T MRI machines. Scans were acquired either free-breathing with navigator-gating or using navigator-gating with fat suppression. The spatial resolution of the scans varied: $1.25 \times 1.25 \times 2.5$ mm, $1.4 \times 1.4 \times 1.4$ mm, or $1.3 \times 1.3 \times 4.0$ mm. Patients underwent MRI scans either before undergoing ablation or between one and six months post-ablation.

2.2.2 2018 Left Atria Segmentation Challenge (LASC) Dataset

The 2018 Left Atria Segmentation Challenge (LASC) concentrated on the segmentation of the LA cavity. The dataset included 100 training images and 54 testing images, all provided with 3D binary masks of the LA cavity. Each LGE-MRI scan featured a spatial resolution of $0.625 \times 0.625 \times 0.625$ mm³, with spatial dimensions of either $576 \times 576 \times 88$ or $640 \times 640 \times 88$ pixels. These clinical images were obtained using either a 1.5 Tesla Avanto or a 3.0 Tesla Verio whole-body scanner (Siemens Medical Solutions, Erlangen, Germany). The LA cavity volumes were meticulously segmented in consensus and agreement by three trained observers, ensuring the provision of high-quality ground truth annotations for both training and evaluation.

2.2.3 Automated Cardiac Diagnosis Challenge (ACDC) 2017 Dataset

The Automated Cardiac Diagnosis Challenge (ACDC) 2017 dataset comprises 150 MRI scans categorized into five subgroups: normal, previous myocardial infarction, dilated cardiomyopathy, hypertrophic cardiomyopathy, and abnormal right ventricle. These scans were collected over six years using two MRI scanners with different magnetic strengths: 1.5 Tesla (Siemens Area, Siemens Medical Solutions, Germany) and 3.0 Tesla (Siemens Trio Tim, Siemens Medical Solutions, Germany). Cine MRI images were acquired under breath-hold conditions using either retrospective or prospective gating, with a steady-state free precession (SSFP) sequence in the short-axis orientation. The scans consist of a series of short-axis slices covering the left ventricle (LV) from base to apex, with a slice thickness of 5 mm (occasionally 8 mm) and sometimes an interslice gap of 5 mm, resulting in images spaced every 5 or 10 mm depending on the examination. The spatial resolution ranges from 1.37 to 1.68 mm²/pixel, and each series includes 28 to 40 images, covering the cardiac cycle completely or partially. The dataset is divided into 100 training images and 50 testing images for the segmentation of the left ventricle (LV), myocardium (MYO), and right ventricle (RV) during both end-systolic (ES) and end-diastolic (ED) phases.

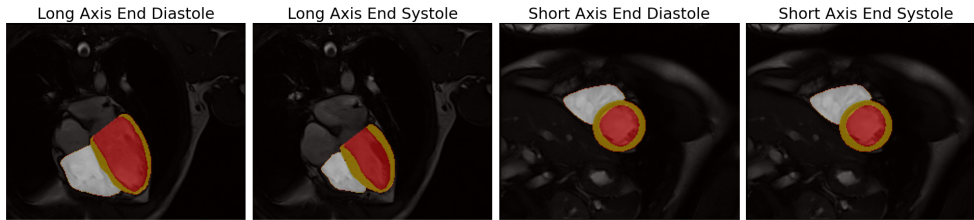


Fig. 1: Visualization of the long axis and short axis views in both end diastole and end systole phases for the MnM2 dataset. The right ventricle (RV) is highlighted in white, the Myocardium (MYO) is highlighted in yellow, and the Left Ventricle (LV) is highlighted in red.

2.2.4 Multi-Centre, Multi-Vendor, and Multi-Disease Cardiac Image Segmentation Challenge (MnM-1 and MnM-2)

The MnM challenge has been conducted twice, first in 2020 (MnM-1) and then in 2021 (MnM-2). MnM-1 included a total of 345 scans, with 209 images designated for training and 136 for testing. Participants were tasked with segmenting the left ventricle (LV), myocardium (MYO), and right ventricle (RV) in both end-systolic (ES) and end-diastolic (ED) phases. The scans were obtained from clinical centres located in three countries (Spain, Germany, and Canada) and utilized four different magnetic resonance scanner vendors: Siemens, General Electric, Philips, and Canon.

MnM-2 provided a training set of 200 images and a testing set of 160 images. Similar to MnM-1, segmentation was required for the LV, MYO, and RV in both ES and ED phases. However, MnM-2 included both Short-Axis (ShA) and long-axis (LoA) views. The LoA view shows the heart from base to apex, essentially cutting the heart vertically, while the ShA view cuts the heart horizontally, perpendicular to the long axis. It shows circular cross-sections of the ventricles. Fig. 1 shows the LoA and ShA for both ES and ED phases. The data for MnM-2 were acquired from clinical centres in Spain using three different MRI scanner vendors: Siemens, General Electric, and Philips.

A summary of the datasets, including labels and the number of training and testing images, are shown in supplementary material Table A1.

2.3 Implementation Details

In this study, we employed nnU-Net, which supports training under five main conditions: 2D, 3D full resolution, 3D low resolution, 3D cascade, and ensemble. However, it was not feasible to evaluate certain datasets using the 3D low-resolution and cascade configurations. For datasets with small image sizes, the U-Net cascade (and consequently the 3D low-resolution configuration) was omitted because the patch size of the full-resolution U-Net already covered a substantial portion of the input images.

The models were trained using an NVIDIA A100 80GB PCIe GPU. The training process spanned 1000 epochs, starting with an initial learning rate of 0.01. We utilised the Stochastic Gradient Descent (SGD) optimiser. To ensure the robustness

Table 1: Performance of LAScarQS (Task 1). The best cavity segmentation values are in **bold**, and the best scar segmentation values are underlined. DSC- Dice Score, HD - Hausdorff Distance, MSD- Mean Surface Distance, HD95-95th percentile of HD.

Model	Label	DSC	Jaccard	HD	MSD	HD95
2D	Cavity	0.926	0.863	12.952	0.805	3.402
	Scar	0.438	0.283	37.166	2.539	13.036
3D full resolution	Cavity	0.939	0.884	12.622	0.666	3.088
	Scar	0.443	0.288	<u>37.060</u>	<u>2.512</u>	12.620
3D low resolution	Cavity	0.937	0.882	13.942	0.711	3.254
	Scar	0.411	0.262	37.294	2.789	13.425
3D cascade	Cavity	0.939	0.885	12.601	0.674	3.138
	Scar	<u>0.449</u>	<u>0.293</u>	38.125	2.530	<u>12.554</u>
Ensemble	Cavity	0.939	0.886	12.486	0.663	3.041
	Scar	0.439	0.285	37.078	2.590	12.850

and reliability of the model’s performance, we used five-fold cross-validation and the test results were obtained using all the five folds as explained in the nnU-Net.

2.4 Evaluation Metrics

To assess the performance of our segmentation models, we employ a comprehensive set of evaluation metrics: Dice Similarity Coefficient (DSC), Jaccard Index, Hausdorff Distance (HD), Mean Surface Distance (MSD), and the 95th percentile Hausdorff Distance (HD95). Each of these metrics provides unique insights into different aspects of the segmentation quality, offering a holistic view of model performance.

3 Results

Here, we present the results of the nnU-Net models on the LAScarQS, LASC, ACDC, MnM, and MnM2 datasets. Note that when comparing with other approaches, the results are reported with the performance of the best-performing method shown first, followed by nnU-Net’s best performance (i.e., the best-performing method vs. nnU-Net’s best performance).

3.1 LAScarQS

In Table 1 and Table 2, we present the performance evaluation of the nnU-Net for Task 1 and Task 2, respectively. Comparative analyses against alternative methods are provided in the supplementary materials, in Table A4 and Table A5. When comparing our methods to others, the LAScarQS Task 1 scar segmentation exhibited the most significant difference, with other methods (DSC - 0.660 to 0.553 vs 0.439 to 0.411) surpassing the nnU-Net models by 21.1%. Additionally, the HD values for scar segmentation are notably higher (Table 1 and supplementary Table A4). This might

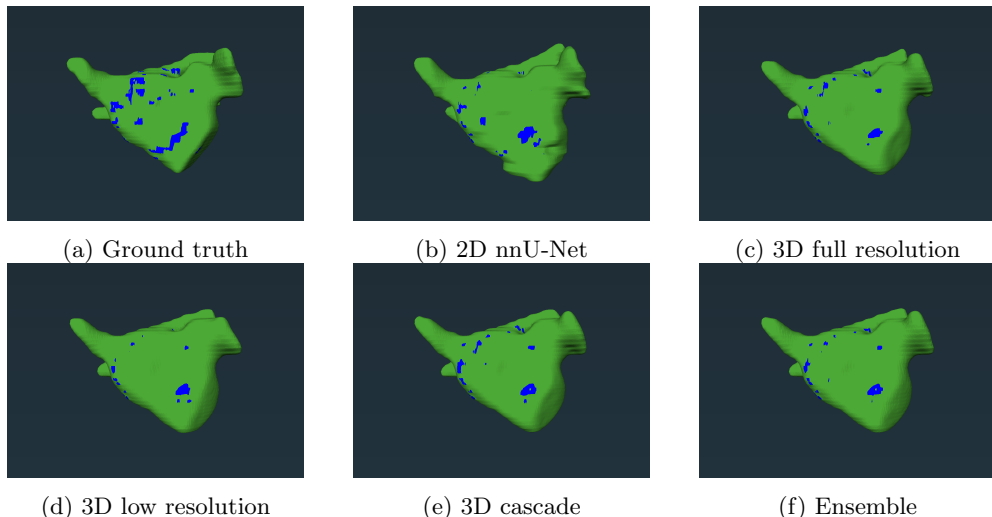


Fig. 2: Comparison of Ground Truth and Predictions from different variations of nnU-Nets for the LAScarQs Task 1. The Left Atrial (LA) cavity is highlighted in green, and LA scars are highlighted in blue. Visualised using Amira 3D software.

Table 2: Performance of LAScarQS (Task 2). The best cavity segmentation values are in **bold**. DSC- Dice Score, HD - Hausdorff Distance, MSD- Mean Surface Distance, HD95-95th percentile of HD

Model	DSC	Jaccard	HD	MSD	HD95
2D	0.930	0.869	13.971	0.733	3.018
3D full resolution	0.937	0.882	12.971	0.672	2.880
3D low resolution	0.935	0.879	12.741	0.692	3.069
3D cascade	0.937	0.882	12.807	0.667	2.746
Ensemble	0.938	0.883	12.767	0.652	2.737

be due to the class imbalance of the scars and cavity (see discussion section for more details).

However, nnU-Net models achieve superior performance in cavity segmentation, despite their lower results in scar segmentation in Task 1 (DSC - 0.875 to 0.938 vs 0.926 to 0.939). This trend is also observed in LAScarQS Task 2 cavity segmentation (Table 2 and supplementary Table A5), where even the nnU-Net (2D) model outperforms other methods (DSC range - 0.872 to 0.929 vs 0.930 to 0.938). In Task 2, the nnU-Net ensemble model achieves the best performance in both Dice score (0.938) and MSD (0.652) metrics, while the nnU-Net (3D low res) model achieves the best performance for HD (12.741). nnU-Net is able to perform competitively even with lesser data compared to other methods in the challenge. The nnU-Net models achieve higher performance metrics not only in dice scores but also in HD and MSD matrices.

Table 3: Performance of LASC dataset. The best cavity segmentation values are in **bold**. DSC- Dice Score, HD - Hausdorff Distance, MSD- Mean Surface Distance, HD95-95th percentile of HD

Model	DSC	Jaccard	HD	MSD	HD95
2D	0.926	0.863	17.583	1.052	3.930
3D full resolution	0.933	0.875	17.485	0.972	3.681
3D low resolution	0.931	0.872	16.877	0.991	3.727
3D cascade	0.933	0.874	17.553	0.984	3.756
Ensemble	0.934	0.877	16.873	0.954	3.628

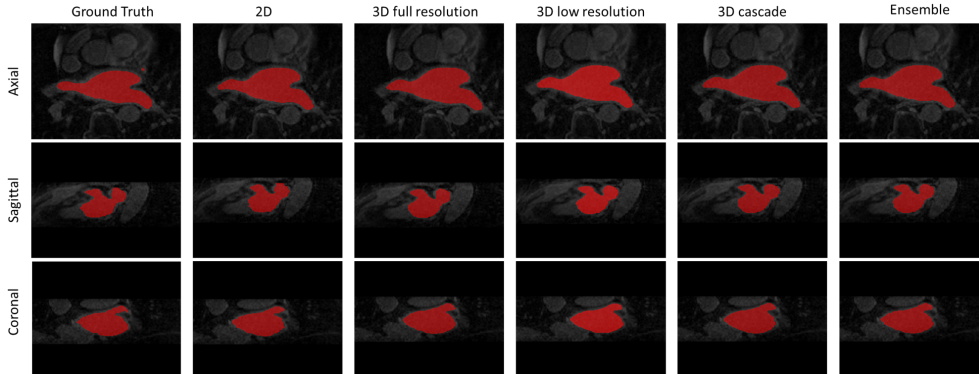


Fig. 3: Comparison of ground truth and predictions from different nnU-Net Versions (2D, 3D Full Resolution, 3D Low Resolution, 3D Cascade, and Ensemble) in three anatomical views: Axial, Sagittal, and Coronal for the LASC dataset. The cavity area is highlighted in Red. Visualized using ITK-SNAP software.

3.2 LASC

For the LASC dataset, the ensemble model achieves the highest performance (DSC - 0.934) (Table 3). According to supplementary Table A6, nnU-Net demonstrates competitive performance with other methods, with only [24] surpassing nnU-Net by 0.1% (DSC range - 0.898 to 0.935 vs 0.923 to 0.934). Interestingly, even the nnU-Net (2D) model shows competitive performance compared to the latest models [25] (DSC in both 0.926). nnU-Net is able to surpass the novel method even without additional configurations. We assess the qualitative performance of the nnU-Nets using ITK-SNAP software [26] as shown in Fig. 3 for axial, sagittal and coronal views.

3.3 ACDC

Performance evaluation of the ACDC dataset is conducted under two main conditions: End-Diastole (ED) and End-Systole (ES) (Table 4). In both cases, overall, the ensemble method demonstrates superior performance compared to other variations of nnU-Nets. Surprisingly, the 2D nnU-Net exhibits better performance in DSC (0.965)

Table 4: Performance of ACDC Dataset for End-Diastole (ED) and End-Systole (ES) phases for 2D, 3D full resolution (3D full.) and Ensemble (Ens.) models. The best values for the Right Ventricle (RV), Myocardium (MYO), and Left Ventricle (LV) are highlighted in **bold**, underline, and *italic*, respectively.

Model	Label	End-Diastole (ED) phase					End-Systole (ES) phase				
		DSC	Jaccard	HD	MSD	HD95	DSC	Jaccard	HD	MSD	HD95
2D	RV	0.942	0.892	10.438	0.467	3.152	0.885	0.799	12.678	0.827	4.318
	MYO	0.897	0.814	10.05	0.331	<u>1.583</u>	0.913	0.841	<u>8.231</u>	<u>0.384</u>	<u>1.975</u>
	LV	<i>0.965</i>	<i>0.933</i>	<i>6.739</i>	<i>0.347</i>	<i>2.350</i>	0.927	0.868	<i>6.795</i>	<i>0.483</i>	<i>2.713</i>
3D full resolution	RV	0.934	0.880	11.494	0.617	3.861	0.882	0.793	12.743	0.911	5.245
	MYO	0.889	0.801	<u>8.057</u>	0.367	2.135	0.906	0.829	8.785	0.456	2.551
	LV	0.959	0.922	8.486	0.443	2.720	0.901	0.831	9.028	0.972	4.968
Ensemble	RV	0.944	0.896	10.716	0.459	3.110	0.892	0.809	12.200	0.751	4.208
	MYO	<u>0.898</u>	<u>0.816</u>	9.884	<u>0.325</u>	1.818	<u>0.915</u>	<u>0.844</u>	8.460	0.384	2.193
	LV	0.963	0.930	9.584	0.404	2.474	<i>0.922</i>	<i>0.861</i>	8.321	0.608	3.477

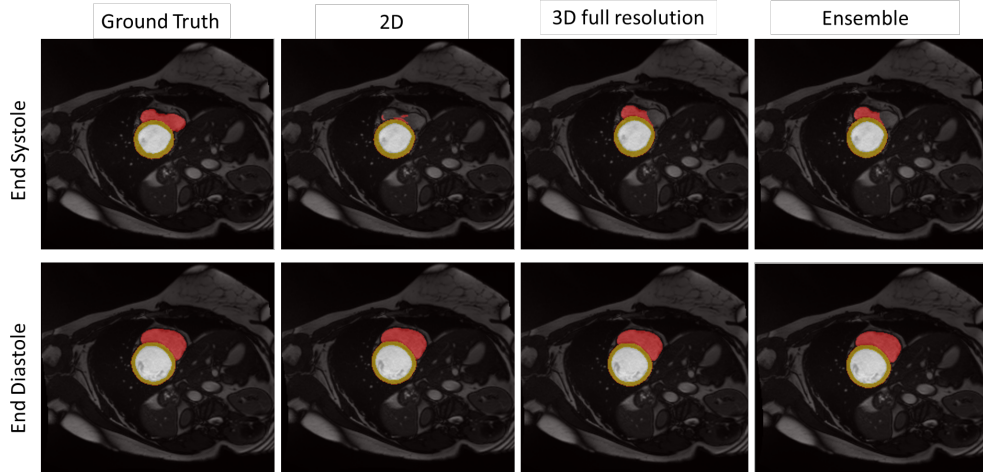


Fig. 4: Comparison of Ground Truth and Predictions from nnU-Net Variants (2D, 3D Full Resolution, and Ensemble) on the ACDC Dataset for End Systole (ES) and End Diastole (ED) Phases. The right ventricle (RV) is highlighted in red, the myocardium (MYO) is in yellow, and the left ventricle (LV) is in white.

than both 3D (0.959) and ensemble (0.963) models in LV segmentation of the ACDC-ED phase. When comparing the ED and ES phases, LV and RV generally perform better in the ED phase than in the ES phase. However, MYO has shown better performance in the ES phase.

When compared to other approaches (Supplementary Table A7), nnU-Net exhibits slightly lower performance across all segmentation tasks relative to other methods tailored to the ACDC dataset. However, the differences in Dice Similarity Coefficient

(DSC) are consistently less than 2% in all cases: LV ED (0.968 vs. 0.965), LV ES (0.938 vs. 0.927), MYO ED (0.906 vs. 0.898), MYO ES (0.923 vs. 0.915), RV ED (0.955 vs. 0.944), and RV ES (0.904 vs. 0.892). Fig. 4 illustrates a performance comparison between the ground truth and predictions generated by nnU-Net (2D), nnU-Net (3D full resolution), and ensemble models for both ED and ES phases.

Table 5: Performance of MnM Dataset for End-Diastole (ED) and End-Systole (ES) phases for 2D, 3D full resolution (3D full.) and Ensemble (Ens.). The best segmentation values for the Left Ventricle (LV), Myocardium (MYO), and Right Ventricle (RV) are highlighted in **bold**, underline, and *italic*, respectively. DSC- Dice Score, HD - Hausdorff Distance, MSD- Mean Surface Distance, HD95-95th percentile of HD, LV- Left Ventricle, MYO- Myocardium, RV- Right Ventricle.

Model	Label	End-Diastole (ED) phase					End-Systole (ES) phase				
		DSC	Jaccard	HD	MSD	HD95	DSC	Jaccard	HD	MSD	HD95
2D	LV	0.936	0.882	7.517	0.728	3.871	0.888	0.833	12.681	2.368	8.513
	MYO	0.824	0.706	10.738	0.592	3.676	0.800	0.689	15.428	1.905	7.304
	RV	0.909	0.836	11.601	0.900	4.578	<i>0.893</i>	<i>0.821</i>	14.595	1.450	6.411
3D full resolution	LV	0.933	0.877	8.199	0.819	4.261	0.909	0.842	8.576	0.944	4.507
	MYO	0.819	0.699	10.776	0.580	3.484	0.841	0.734	11.141	0.812	3.952
	RV	0.908	0.836	11.520	0.870	4.501	0.871	0.784	13.130	1.258	5.673
Ensemble	LV	0.937	0.883	7.393	0.725	3.761	0.888	0.803	8.486	0.956	4.432
	MYO	<u>0.826</u>	<u>0.709</u>	<u>9.944</u>	<u>0.527</u>	<u>3.138</u>	<u>0.864</u>	<u>0.762</u>	<u>9.872</u>	<u>0.613</u>	<u>3.542</u>
	RV	<i>0.913</i>	<i>0.843</i>	<i>10.847</i>	<i>0.818</i>	<i>4.208</i>	0.852	0.751	<i>12.658</i>	<i>1.083</i>	<i>5.366</i>

3.4 MnM

As in the ACDC dataset, MnM performance is evaluated on both ES and ED (Table 5) phases. The 2D nnU-Net (DSC-0.893) outperforms both 3D (DSC-0.871) and ensemble models (DSC-0.852) in RV segmentation in the ES phase, while the 3D full-resolution model also outperforms LV segmentation in terms of dice score in the ES phase (0.888 vs 0.909). In the ED phase, the ensemble model demonstrates superior performance (DSC - 0.937, HD 7.4). RV segmentation in both phases achieves higher dice scores (ED - 0.552 to 0.910 vs 0.908 to 0.913, ES - 0.517 to 0.860 vs 0.852 to 0.871) compared to other approaches (supplementary Table A8). In other cases, other approaches surpass the nnU-Net by slight margins, typically less than 1% in DSC (LV (ED)-0.940 vs 0.937, MYO (ED) - 0.839 to 0.826, MYO (ES) - 0.870-0.864). Similar to the ACDC dataset, MnM also shows better performance in LV and RV in the ED phase especially in DSC and Jaccard values compared to the ES phase. However, MYO has shown better performance in the ES phase in generally. In Fig. 5, we compare the performance of the nnU-Net models in both ES and ED phases.

3.5 MnM2

Deviating from the MnM challenge, we analyze the performance of the MnM2 challenge in four different conditions: Short Axis (ShA) ED phase, ShA ES phase (Table 6),

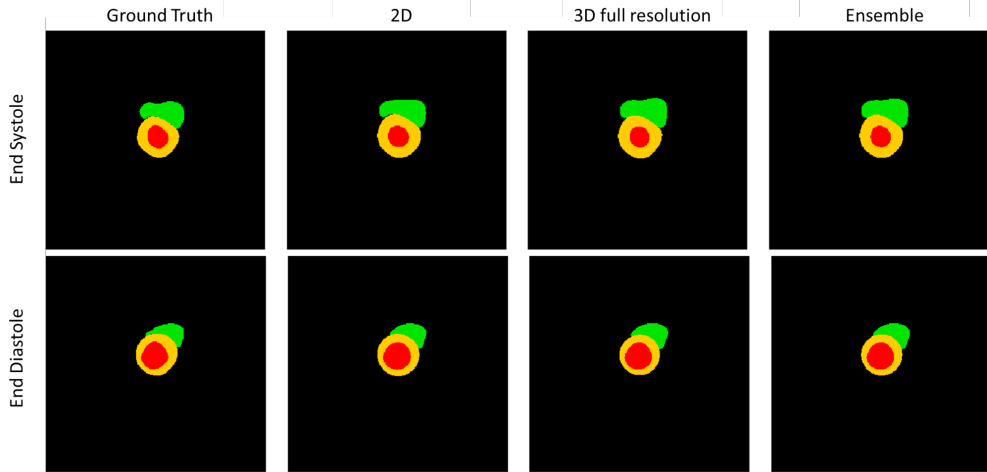


Fig. 5: Comparison of Ground Truth and Predictions from nnU-Net Variants (2D, 3D Full Resolution, and Ensemble) on the MnM Dataset for End Systole (ES) and End Diastole (ED) Phases. The right ventricle (RV) is highlighted in green, the myocardium (MYO) is in yellow, and the left ventricle (LV) is in red.

Table 6: Performance of **MnM2** Dataset for Short Axis (ShA) End-Diastole (ED) and End-Systole (ES) phases for 2D, 3D full resolution (3D full.) and Ensemble (Ens.) . The best segmentation values for the Left Ventricle (LV), Myocardium (MYO), and Right Ventricle (RV) are highlighted in **bold**, underline, and *italic*, respectively. DSC- Dice Score, HD - Hausdorff Distance, MSD- Mean Surface Distance, HD95-95th percentile of HD, LV- Left Ventricle, MYO- Myocardium, RV- Right Ventricle.

Model	Label	End-Diastole (ED) phase					End-Systole (ES) phase				
		DSC	Jaccard	HD	MSD	HD95	DSC	Jaccard	HD	MSD	HD95
2D	LV	0.957	0.920	8.268	0.515	3.170	0.958	0.920	8.350	0.513	3.170
	MYO	0.867	0.769	12.238	0.442	2.842	0.867	0.770	11.928	0.428	2.571
	RV	0.934	0.879	<i>10.050</i>	0.766	4.084	0.934	0.879	11.228	0.817	4.520
3D full resolution	LV	0.955	0.916	8.361	0.565	3.571	0.956	0.916	8.233	0.561	3.481
	MYO	0.862	0.761	12.035	0.426	2.561	0.862	0.761	12.004	0.426	2.555
	RV	0.934	0.878	10.394	0.779	4.200	0.934	0.878	<i>10.301</i>	0.779	4.302
Ensemble	LV	0.958	0.921	8.029	0.496	3.256	0.958	0.920	8.225	0.503	3.264
	MYO	<u>0.869</u>	<u>0.772</u>	<u>11.492</u>	<u>0.396</u>	<u>2.371</u>	<u>0.868</u>	<u>0.771</u>	<u>11.684</u>	<u>0.398</u>	<u>2.341</u>
	RV	<i>0.937</i>	<i>0.884</i>	11.079	<i>0.742</i>	<i>4.021</i>	<i>0.938</i>	<i>0.885</i>	11.119	<i>0.722</i>	<i>3.930</i>

Long Axis (LoA) ED phase and LoA ES phase (Table 7). In both phases in ShA, the ensemble method demonstrates superior performance (DSC-0.937). For LoA segmentation, images have the shape of $H \times W \times 1$, indicating only one layer in the Z-axis, making the 3D full-resolution method particularly effective, and thus only 3D full-resolution results are reported. The challenge organizers report only the values of RV

Table 7: Performance of **MnM2** Dataset for Long Axis (LoA) End-Diastole (ED) and End-Systole (ES) phases for 3D full resolution only.

Label	End-Diastole (ED) phase					End-Systole (ES) phase				
	DSC	Jaccard	HD	MSD	HD95	DSC	Jaccard	HD	MSD	HD95
LV	0.968	0.938	4.082	0.871	2.977	0.948	0.904	4.432	1.076	3.246
MYO	0.878	0.786	6.504	0.662	2.151	0.891	0.809	5.342	0.837	2.809
RV	0.934	0.878	6.055	1.262	4.075	0.899	0.822	6.108	1.457	4.254

Table 8: Comparison of Dice scores of nnUnet and Other methods. ED - End Diastole, ES - End Systole, ShA- Short Axis, LoA - Long Axis, LV - Left Ventricle, MYO - Myocardium, RV - Right Ventricle, LA - Left Atrium.

Dataset	Sub task	Label	nnU-Net	Other Methods	Abs Difference (%)
ACDC	ED	LV	0.965	0.968	0.3
	ES		0.927	0.938	1.1
	ED	MYO	0.898	0.906	0.8
	ES		0.915	0.923	0.8
	ED	RV	0.944	0.955	1.1
	ES		0.892	0.904	1.2
LAScarQS	Task-1	LA Scar	0.449	0.660	21.1
	Task-1	LA Cavity	0.939	0.938	0.1
	Task-2	LA Cavity	0.938	0.929	0.9
MnM1	ED	LV	0.937	0.940	0.3
	ES		0.909	0.890	1.9
	ED	MYO	0.826	0.834	0.8
	ES		0.864	0.870	0.6
	ED	RV	0.913	0.910	0.3
	ES		0.893	0.860	3.3
MnM2	ShA ED	RV	0.937	0.940	0.3
	ShA ES		0.938	0.914	2.4
	LoA ES		0.934	0.935	0.1
	LoA ED		0.900	0.905	0.5
LASC	-	LA Cavity	0.934	0.935	0.1

segmentation (Table A9). In this case, nnU-Net outperforms ShA ES segmentation by 2.4% compared to other models in DSC (0.914 vs 0.938). However, in other cases (ShA ED (0.940 vs 0.937), LoA ES (0.905 vs 0.900), and LoA ED (0.935 vs 0.934)), other models surpass the nnU-Net, but the margin is less than 1%. In the ShA view, both ED and ES have similar performance in DSC and Jaccard while in LoA, overall LV and RV have better results in the ED phase compared to the ES phase and MYO has better performance in the ES phase compared to the ED phase.

In summary, ensemble models demonstrate strong performance across all datasets. Surprisingly, in some cases, the 2D models outperform the 3D models and even the

ensemble models. The most significant difference where other models surpass nnU-Net occurs in the LAScarQs Task 1 scar segmentation. A summary of the comparison between the highest Dice value obtained from nnU-Net, the highest Dice value from other methods, and the absolute difference (%) is shown in Table 8.

4 Discussion

In this section, we discuss and analyze our findings in detail.

4.1 Lower performance in LAScarQS scar segmentation

In analyzing the performance of nnU-Net for scar segmentation in the LAScarQS Task 1, it is evident that the nnU-Net underperforms relative to other models. Several factors contribute to this discrepancy. Firstly, the primary challenge lies in the nature of the target region. Scar tissues occupy only a small fraction of the LA compared to the LA cavity (As shown in Fig. A1 in supplementary nearly 0.7% occupies the cavity, and less than 0.1% occupies the scar). This significant imbalance in the spatial distribution makes it difficult for the model to accurately distinguish and segment the scar regions. The nnU-Net’s architecture, while robust for larger and more continuous regions, struggles with the precision required for such minute and sparse areas.

Secondly, the characteristics of the data further complicate the task. Unlike the LA cavity, which presents as a more continuous and homogenous region, scar tissues are often irregular and dispersed. This non-continuous nature of scar data poses a substantial challenge for segmentation models, particularly those like nnU-Net, which rely heavily on spatial continuity and context provided by larger regions.

Additionally, most state-of-the-art methods for scar segmentation adopt a two-stage network approach. These approaches typically involve an initial stage that performs coarse segmentation, identifying potential regions of interest (ROIs), followed by a refinement stage that focuses on enhancing the segmentation accuracy within these regions. This two-step process allows for more focused learning and better handling of small and irregular regions, leading to superior performance in scar segmentation tasks. In contrast, the nnU-Net framework primarily utilizes a single-stage approach. While this method is advantageous for its simplicity and reduced computational requirements, it may not provide the necessary granularity and focus required for effectively segmenting small and irregular structures like scar tissues. The lack of an initial coarse segmentation stage means that nnU-Net must rely solely on its inherent ability to capture and distinguish fine details within a single pass, which is inherently more challenging for such complex tasks.

Moreover, the non-continuous property of the scar tissue can contribute to higher HD values. The HD metric is particularly sensitive to outliers and disjoint regions, which are characteristic of scar tissue. As a result, even small segmentation errors can lead to disproportionately high HD values, further reflecting the difficulty in accurately segmenting these regions.

4.2 Ensemble Results

When comparing nnU-Net ensemble models to individual 3D and 2D nnU-Net variants, it is essential to understand that while ensemble methods have the potential to enhance model performance, this improvement is not always guaranteed. For an ensemble to significantly outperform a single model, the base classifiers must exhibit diversity. This means they need to make different errors, thereby complementing each other’s weaknesses. However, when the signal in the data is dominated by a few strong predictors, most models, including those within an ensemble, will likely capture and model this dominant information similarly. This can result in highly correlated predictions across the ensemble members, thereby reducing the potential benefits of combining them. In other words, if the nnU-Net ensemble models demonstrate lower performance compared to individual 3D or 2D nnU-Net variants, a lack of diversity among the ensemble members could be a contributing factor. When ensemble models are not sufficiently diverse, they may fail to provide the expected performance boost, leading to a situation where the ensemble’s performance is merely on par with or even inferior to the best individual model.

4.3 Higher performance in 2D model compared to 3D model

In our analysis of the ACDC, MnM, and MnM2 datasets, we observe a trend where 2D nnU-Net implementations demonstrated superior performance, as measured by Dice scores, compared to their 3D counterparts. While no significant differences (all statistical tests were conducted using the Wilcoxon test) were observed between 2D and 3D nnU-Net implementations for LV and RV segmentation, the MYO shows statistically significant results in those configurations. Specifically, differences were observed in ACDC (ED and ES phases), the MnM (ED phase) and the MnM2(ES phase). There was no statistical significance in the MnM-ES phase and MnM2-ED phase even though the 2D model shows a higher dice score. These results suggest that the myocardium poses unique challenges and opportunities for segmentation, distinguishing it from the LV and RV.

One of the main reasons would be the myocardium’s structure and imaging characteristics, which make its segmentation inherently different from that of the LV and RV. Unlike the LV and RV, which are more clearly defined by their lumen boundaries, the myocardium often has less distinct edges due to variability in contrast and partial volume effects. This nuanced texture and boundary information may favour the use of simpler 2D architectures, which can focus on in-plane details without being overwhelmed by 3D spatial relationships that may introduce noise.

Also, MRI data typically exhibit high in-plane resolution but lower through-plane resolution. For the myocardium, where subtle edge and texture features are critical for accurate segmentation, the higher in-plane resolution plays a key role. 2D models excel in leveraging these high-resolution details, whereas 3D models may struggle to integrate lower-resolution through-plane information effectively.

3D models, by their nature, require more parameters and training data to generalize effectively. This requirement becomes particularly challenging for the myocardium, where segmentation demands a fine-grained understanding of complex features. In

cases where the dataset size is limited, 2D models may achieve better generalization due to their lower parameter count and simpler optimization landscape.

Furthermore, the nature of the segmentation task itself may favour 2D approaches. If the key features for accurate segmentation are predominantly visible within individual slices, the additional complexity introduced by 3D models in capturing inter-slice relationships may not provide significant benefits. In fact, this added complexity could potentially introduce noise or irrelevant information into the learning process, leading to suboptimal performance.

4.4 Effect of the configurations of nnU-Net

When utilizing nnU-Net, the selection of loss functions, optimizers, batch sizes, and patch sizes is tailored to the specific characteristics of the dataset. In our case, all the nnU-Nets employ a combination of Dice loss and cross-entropy loss (DiceCE loss) as its default loss function. However, in scenarios with class imbalance, alternative loss functions such as DiceHD loss (combining Dice loss with Hausdorff Distance loss) and DiceFocal loss (combining Dice loss with focal loss) have demonstrated superior performance [27]. Therefore, incorporating these loss functions into nnU-Net could potentially enhance segmentation results.

Furthermore, nnU-Net traditionally utilises the SGD optimizer. Nonetheless, recent studies have shown that the Adam optimizer can achieve comparable, if not superior, outcomes in segmentation tasks [28]. Consequently, integrating the Adam optimizer into nnU-Net’s framework may lead to improved performance in certain cases.

4.5 Performance Differences in End Systole and End Diastole Phases

The results indicate that for the ACDC and MnM datasets, the LV and RV exhibit better segmentation performance during the End-Diastole (ED) phase, particularly in Dice and Jaccard scores. In contrast, the Myocardium (MYO) achieves better segmentation performance during the End-Systole (ES) phase.

In the ED phase, both LV and RV are at their maximum size due to blood filling, which results in more distinct boundaries and reduced segmentation errors. Larger structures with smoother curvature and higher contrast against surrounding tissues are generally easier to segment. Additionally, the heart experiences reduced motion artifacts during ED due to slower movement, further improving segmentation accuracy. Conversely, during the ES phase, the ventricles contract and become smaller, leading to less distinct boundaries and increased structural deformation. These factors introduce variability that complicates the segmentation task for the LV and RV.

However, the MYO achieves better segmentation in the ES phase, primarily due to its increased thickness during contraction. The enhanced visibility and prominence of the thickened myocardium, along with its well-defined boundaries, aid in achieving higher segmentation accuracy. In contrast, during the ED phase, the thinner myocardium has less distinct boundaries, making it more challenging to segment accurately.

For the MnM2 dataset, the segmentation performance in ED and ES phases is comparable, particularly in Dice and Jaccard scores. This consistency can be attributed to the imaging modality, which captures the heart in the ShA view. In this view, the heart’s structures, including the LV, RV, and MYO, maintain relatively similar cross-sectional shapes across both phases. Volume changes during the cardiac cycle predominantly occur along the long axis (apex-base direction), which is less apparent in the Short Axis view. This uniformity reduces structural distortions and phase-dependent variability.

4.6 Limitations of the Study

This study primarily focused on cardiac-related datasets and utilized a single imaging modality, namely cardiac MRI. While this approach allowed for a detailed evaluation of nnU-Net’s performance in a specific domain, it limits the generalizability of the findings. Future research should extend this work to encompass other anatomical regions, such as the brain and abdomen, which are commonly studied in medical imaging. Additionally, incorporating other imaging modalities, including computed tomography (CT), X-ray, and ultrasound, would provide a broader validation of nnU-Net’s robustness and highlight its applicability across diverse clinical scenarios. Exploring these modalities could uncover unique challenges or advantages specific to nnU-Net’s architecture when applied to different data types.

Another limitation is the study’s focus on the baseline nnU-Net architecture without exploring existing variations or improvements made by other researchers [18, 29]. Evaluating these architectural enhancements could provide valuable insights into their impact on segmentation performance and computational efficiency, thereby enriching the comparative analysis.

Moreover, this study exclusively relied on publicly available datasets that are widely used within the research community. While this ensures reproducibility and relevance, the findings may not fully represent the challenges encountered in real-world clinical data, which can vary significantly in terms of quality, resolution, and heterogeneity. Future studies could benefit from incorporating private datasets or datasets with more diverse patient populations and imaging conditions to better understand nnU-Net’s performance in clinical practice.

Finally, our study did not focus on ventricular scars. Ventricular scar segmentation is crucial for many clinical applications, such as planning cardiac ablation procedures and assessing myocardial viability. Future work could explore this aspect in greater depth, utilizing dedicated datasets and task-specific modifications to evaluate nnU-Net’s capability to handle these clinically significant tasks.

5 Conclusion

In this study, we evaluated the performance of five cardiac MRI segmentation datasets using various adaptations of nnU-Net. Through over 130 training cycles, we conducted an extensive performance analysis of these models. Our comparative study with existing methods demonstrated that nnU-Net not only performs competitively but often

surpasses state-of-the-art techniques, even outperforming the latest methods on certain datasets.

The findings highlight the robustness and adaptability of nnU-Net for cardiac MRI segmentation tasks. Its consistent performance across diverse datasets underscores its potential as a reliable tool for clinical applications. However, this study raises an important question: when is it necessary to develop task-specific models for particular cardiac segmentation challenges?

The answer lies in the specific requirements and complexities of individual tasks. While nnU-Net provides a strong baseline, certain scenarios may demand customized solutions. For example, while nnU-Net excels in segmenting larger anatomical structures such as the LA cavity, LV, and RV, its performance in segmenting more intricate regions, such as the MYO and scars, is relatively lower. In such cases, developing specialized models can lead to improved outcomes. Furthermore, integrating data from multiple imaging modalities (e.g., MRI and CT) may require tailored approaches to effectively interpret and merge the information.

In conclusion, while nnU-Net offers a robust and versatile foundation for cardiac MRI segmentation, the development of specialized models tailored to specific clinical challenges remains essential. This study demonstrates that while general-purpose frameworks like nnU-Net provide significant advantages, there is a critical need for continued innovation and customization to address the unique complexities of various medical imaging tasks. Future research should prioritize the exploration and development of these specialized approaches to fully leverage the potential of deep learning in medical imaging.

6 List of abbreviations

- CVD - Cardiovascular diseases
- AF - Atrial Fibrillation
- MRI - Magnetic Resonance Imaging
- LA - Left Atria
- MYO - Myocardium
- RA - Right Atria
- LV - Left Ventricle
- RV - Right Ventricle
- ES - End Systole
- ED - End Diastole
- ShA - Short Axis
- LoA - Long Axis
- DSC - Dice Score
- HD - Hausdorff Distance
- MSD - Mean Surface Distance

7 Declarations

7.1 Ethics approval and consent to participate

Not applicable

7.2 Consent for publication

Not applicable

7.3 Availability of data and materials

The datasets analysed during the current study are publically available in the following repositories except for the LAScarQs 2022 dataset [19], which was obtained from the corresponding authors of the challenge.

LASC [20]:- <https://www.cardiacatlas.org/atriaseg2018-challenge/atria-seg-data/>

ACDC [21]:- <https://www.creatis.insa-lyon.fr/Challenge/acdc/databases.html>

MnM1 [22]:- <https://www.ub.edu/mnms/>

MnM2 [23]:- <https://www.ub.edu/mnms-2/>

7.4 Competing Interests

Not applicable

7.5 Funding

Not applicable

7.6 Author contributions

MG is the main author of the paper, who conducted the experiments and wrote the manuscript. FX contributed by conducting experiments and preparing tables. JZ served as the research advisor and prepared figures. All authors review the article.

7.7 Acknowledgements

Not applicable

References

- [1] Tsao, C.W., Aday, A.W., Almarzooq, Z.I., Anderson, C.A., Arora, P., Avery, C.L., Baker-Smith, C.M., Beaton, A.Z., Boehme, A.K., Buxton, A.E., *et al.*: Heart disease and stroke statistics—2023 update: a report from the american heart association. *Circulation* **147**(8), 93–621 (2023)
- [2] Allesie, M., Ausma, J., Schotten, U.: Electrical, contractile and structural remodeling during atrial fibrillation. *Cardiovascular research* **54**(2), 230–246 (2002)

- [3] Boldt, A., Wetzel, U., Lauschke, J., Weigl, J., Gummert, J., Hindricks, G., Kottkamp, H., Dhein, S.: Fibrosis in left atrial tissue of patients with atrial fibrillation with and without underlying mitral valve disease. *Heart* **90**(4), 400–405 (2004)
- [4] Gunawardhana, M., Kulathilaka, A., Zhao, J.: Integrating deep learning in cardiology: A comprehensive review of atrial fibrillation, left atrial scar segmentation, and the frontiers of state-of-the-art techniques. arXiv preprint arXiv:2407.09561 (2024)
- [5] Ukwatta, E., Arevalo, H., Rajchl, M., White, J., Pashakhanloo, F., Prakosa, A., Herzka, D.A., McVeigh, E., Lardo, A.C., Trayanova, N.A., *et al.*: Image-based reconstruction of three-dimensional myocardial infarct geometry for patient-specific modeling of cardiac electrophysiology. *Medical physics* **42**(8), 4579–4590 (2015)
- [6] Vergara, G.R., Marrouche, N.F.: Tailored management of atrial fibrillation using a lge-mri based model: from the clinic to the electrophysiology laboratory. *Journal of cardiovascular electrophysiology* **22**(4), 481–487 (2011)
- [7] Peters, D.C., Wylie, J.V., Hauser, T.H., Kissinger, K.V., Botnar, R.M., Essebag, V., Josephson, M.E., Manning, W.J.: Detection of pulmonary vein and left atrial scar after catheter ablation with three-dimensional navigator-gated delayed enhancement mr imaging: initial experience. *Radiology* **243**(3), 690–695 (2007)
- [8] Akkaya, M., Higuchi, K., Koopmann, M., Burgon, N., Erdogan, E., Damal, K., Kholmovski, E., McGann, C., Marrouche, N.F.: Relationship between left atrial tissue structural remodelling detected using late gadolinium enhancement mri and left ventricular hypertrophy in patients with atrial fibrillation. *Europace* **15**(12), 1725–1732 (2013)
- [9] Bisbal, F., Guiu, E., Cabanas-Grandío, P., Berruezo, A., Prat-Gonzalez, S., Vidal, B., Garrido, C., Andreu, D., Fernandez-Armenta, J., Tolosana, J.M., *et al.*: Cmr-guided approach to localize and ablate gaps in repeat af ablation procedure. *JACC: Cardiovascular Imaging* **7**(7), 653–663 (2014)
- [10] Tobon-Gomez, C., Geers, A.J., Peters, J., Weese, J., Pinto, K., Karim, R., Ammar, M., Daoudi, A., Margeta, J., Sandoval, Z., *et al.*: Benchmark for algorithms segmenting the left atrium from 3d ct and mri datasets. *IEEE transactions on medical imaging* **34**(7), 1460–1473 (2015)
- [11] Yang, X., Wang, N., Wang, Y., Wang, X., Nezafat, R., Ni, D., Heng, P.-A.: Combating uncertainty with novel losses for automatic left atrium segmentation. In: *Statistical Atlases and Computational Models of the Heart. Atrial Segmentation and LV Quantification Challenges: 9th International Workshop, STACOM 2018, Held in Conjunction with MICCAI 2018, Granada, Spain, September 16,*

2018, Revised Selected Papers 9, pp. 246–254 (2019). Springer

- [12] Arega, T.W., Bricq, S., Meriaudeau, F.: Using polynomial loss and uncertainty information for robust left atrial and scar quantification and segmentation. In: Challenge on Left Atrial and Scar Quantification and Segmentation, pp. 133–144. Springer, ??? (2022)
- [13] Shi, Z., Jiang, M., Li, Y., Wei, B., Wang, Z., Wu, Y., Tan, T., Yang, G.: Mlc: Multi-level consistency learning for semi-supervised left atrium segmentation. *Expert Systems with Applications* **244**, 122903 (2024)
- [14] Mazher, M., Qayyum, A., Abdel-Nasser, M., Puig, D.: Automatic semi-supervised left atrial segmentation using deep-supervision 3dresunet with pseudo labeling approach for lascarqs 2022 challenge. In: Challenge on Left Atrial and Scar Quantification and Segmentation, pp. 153–161. Springer, ??? (2022)
- [15] Jiang, L., Li, Y., Wang, Y., Cui, H., Xia, Y., Zhang, Y.: Deep u-net architecture with curriculum learning for left atrial segmentation. In: Challenge on Left Atrial and Scar Quantification and Segmentation, pp. 115–123. Springer, ??? (2022)
- [16] Chen, C., Bai, W., Rueckert, D.: Multi-task learning for left atrial segmentation on ge-mri. In: Statistical Atlases and Computational Models of the Heart. Atrial Segmentation and LV Quantification Challenges: 9th International Workshop, STACOM 2018, Held in Conjunction with MICCAI 2018, Granada, Spain, September 16, 2018, Revised Selected Papers 9, pp. 292–301 (2019). Springer
- [17] Isensee, F., Jaeger, P.F., Kohl, S.A., Petersen, J., Maier-Hein, K.H.: nnu-net: a self-configuring method for deep learning-based biomedical image segmentation. *Nature methods* **18**(2), 203–211 (2021)
- [18] Isensee, F., Wald, T., Ulrich, C., Baumgartner, M., Roy, S., Maier-Hein, K., Jaeger, P.F.: nnu-net revisited: A call for rigorous validation in 3d medical image segmentation. arXiv preprint arXiv:2404.09556 (2024)
- [19] Zhuang, X., Li, L., Wang, S., Wu, F.: Left Atrial and Scar Quantification and Segmentation: First Challenge, LAScarQS 2022, Held in Conjunction with MICCAI 2022, Singapore, September 18, 2022, Proceedings vol. 13586. Springer, ??? (2023)
- [20] Xiong, Z., Xia, Q., Hu, Z., Huang, N., Bian, C., Zheng, Y., Vesal, S., Ravikumar, N., Maier, A., Yang, X., *et al.*: A global benchmark of algorithms for segmenting the left atrium from late gadolinium-enhanced cardiac magnetic resonance imaging. *Medical image analysis* **67**, 101832 (2021)
- [21] Bernard, O., Lalande, A., Zotti, C., Cervenansky, F., Yang, X., Heng, P.-A., Cetin, I., Lekadir, K., Camara, O., Ballester, M.A.G., *et al.*: Deep learning techniques for automatic mri cardiac multi-structures segmentation and diagnosis: is

- the problem solved? IEEE transactions on medical imaging **37**(11), 2514–2525 (2018)
- [22] Campello, V.M., Gkontra, P., Izquierdo, C., Martín-Isla, C., Sojoudi, A., Full, P.M., Maier-Hein, K., Zhang, Y., He, Z., Ma, J., *et al.*: Multi-centre, multi-vendor and multi-disease cardiac segmentation: the m&ms challenge. IEEE Transactions on Medical Imaging **40**(12), 3543–3554 (2021)
- [23] Martín-Isla, C., Campello, V.M., Izquierdo, C., Kushibar, K., Sendra-Balcells, C., Gkontra, P., Sojoudi, A., Fulton, M.J., Arega, T.W., Punithakumar, K., *et al.*: Deep learning segmentation of the right ventricle in cardiac mri: The m&ms challenge. IEEE Journal of Biomedical and Health Informatics **27**(7), 3302–3313 (2023)
- [24] Singh, K.R., Sharma, A., Singh, G.K.: Attention-guided residual w-net for supervised cardiac magnetic resonance imaging segmentation. Biomedical Signal Processing and Control **86**, 105177 (2023)
- [25] Xu, F., Tu, W., Feng, F., Gunawardhana, M., Yang, J., Gu, Y., Zhao, J.: Dynamic position transformation and boundary refinement network for left atrial segmentation. In: International Conference on Medical Image Computing and Computer-Assisted Intervention (2024). Springer
- [26] Yushkevich, P.A., Gao, Y., Gerig, G.: Itk-snap: An interactive tool for semi-automatic segmentation of multi-modality biomedical images. In: 2016 38th Annual International Conference of the IEEE Engineering in Medicine and Biology Society (EMBC), pp. 3342–3345 (2016). IEEE
- [27] Ma, J., Chen, J., Ng, M., Huang, R., Li, Y., Li, C., Yang, X., Martel, A.L.: Loss odyssey in medical image segmentation. Medical Image Analysis **71**, 102035 (2021)
- [28] Rajinikanth, V., Kadry, S., Damaševičius, R., Sankaran, D., Mohammed, M.A., Chander, S.: Skin melanoma segmentation using vgg-unet with adam/sgd optimizer: a study. In: 2022 Third International Conference on Intelligent Computing Instrumentation and Control Technologies (ICICICT), pp. 982–986 (2022). IEEE
- [29] Jahromi, M.N., Marques, A.D., Ahmed, M., Liu, Z.-Q., Hannum, A.J., Ennis, D.B., Perotti, L.E., Wu, D.: An nnu-net model to enhance segmentation of cardiac cine dense-mri using phase information. In: 2024 IEEE 12th International Conference on Healthcare Informatics (ICHI), pp. 670–673 (2024). IEEE
- [30] Zhang, Y., Meng, Y., Zheng, Y.: Automatically segment the left atrium and scars from lge-mris using a boundary-focused nnu-net. In: Challenge on Left Atrial and Scar Quantification and Segmentation, pp. 49–59. Springer, ??? (2022)

- [31] Lefebvre, A.L., Yamamoto, C.A., Shade, J.K., Bradley, R.P., Yu, R.A., Ali, R.L., Popescu, D.M., Prakosa, A., Kholmovski, E.G., Trayanova, N.A.: Lassnet: A four steps deep neural network for left atrial segmentation and scar quantification. In: Challenge on Left Atrial and Scar Quantification and Segmentation, pp. 1–15. Springer, ??? (2022)
- [32] Tu, C., Huang, Z., Deng, Z., Yang, Y., Ma, C., He, J., Ye, J., Wang, H., Ding, X.: Self pre-training with single-scale adapter for left atrial segmentation. In: Challenge on Left Atrial and Scar Quantification and Segmentation, pp. 24–35. Springer, ??? (2022)
- [33] Liu, T., Hou, S., Zhu, J., Zhao, Z., Jiang, H.: Ugformer for robust left atrium and scar segmentation across scanners. In: Challenge on Left Atrial and Scar Quantification and Segmentation, pp. 36–48. Springer, ??? (2022)
- [34] Zhang, X., Yang, X., Huang, L., Huang, L.: Two stage of histogram matching augmentation for domain generalization: Application to left atrial segmentation. In: Challenge on Left Atrial and Scar Quantification and Segmentation, pp. 60–68. Springer, ??? (2022)
- [35] Khan, A., Alwazzan, O., Benning, M., Slabaugh, G.: Sequential segmentation of the left atrium and atrial scars using a multi-scale weight sharing network and boundary-based processing. In: Challenge on Left Atrial and Scar Quantification and Segmentation, pp. 69–82. Springer, ??? (2022)
- [36] Xie, T., Yang, Z., Yu, H.: La-hrnet: High-resolution network for automatic left atrial segmentation in multi-center leg mri. In: Challenge on Left Atrial and Scar Quantification and Segmentation, pp. 83–92. Springer, ??? (2022)
- [37] Zhou, S., Wang, K.-N., Zhou, G.-Q.: Edge-enhanced feature guided joint segmentation of left atrial and scars in lge mri images. In: Challenge on Left Atrial and Scar Quantification and Segmentation, pp. 93–105. Springer, ??? (2022)
- [38] Li, F., Li, W.: Cross-domain segmentation of left atrium based on multi-scale decision level fusion. In: Challenge on Left Atrial and Scar Quantification and Segmentation, pp. 124–132. Springer, ??? (2022)
- [39] Singh, K.R., Sharma, A., Singh, G.K.: Madru-net: Multi-scale attention-based cardiac mri segmentation using deep residual u-net. *IEEE Transactions on Instrumentation and Measurement* (2023)
- [40] Xia, Q., Yao, Y., Hu, Z., Hao, A.: Automatic 3d atrial segmentation from gemris using volumetric fully convolutional networks. In: *Statistical Atlases and Computational Models of the Heart. Atrial Segmentation and LV Quantification Challenges: 9th International Workshop, STACOM 2018, Held in Conjunction with MICCAI 2018, Granada, Spain, September 16, 2018, Revised Selected Papers 9*, pp. 211–220 (2019). Springer

- [41] Bian, C., Yang, X., Ma, J., Zheng, S., Liu, Y.-A., Nezafat, R., Heng, P.-A., Zheng, Y.: Pyramid network with online hard example mining for accurate left atrium segmentation. In: International Workshop on Statistical Atlases and Computational Models of the Heart, pp. 237–245 (2018). Springer
- [42] Vesal, S., Ravikumar, N., Maier, A.: Dilated convolutions in neural networks for left atrial segmentation in 3d gadolinium enhanced-mri. In: Statistical Atlases and Computational Models of the Heart. Atrial Segmentation and LV Quantification Challenges: 9th International Workshop, STACOM 2018, Held in Conjunction with MICCAI 2018, Granada, Spain, September 16, 2018, Revised Selected Papers 9, pp. 319–328 (2019). Springer
- [43] Li, C., Tong, Q., Liao, X., Si, W., Sun, Y., Wang, Q., Heng, P.-A.: Attention based hierarchical aggregation network for 3d left atrial segmentation. In: Statistical Atlases and Computational Models of the Heart. Atrial Segmentation and LV Quantification Challenges: 9th International Workshop, STACOM 2018, Held in Conjunction with MICCAI 2018, Granada, Spain, September 16, 2018, Revised Selected Papers 9, pp. 255–264 (2019). Springer
- [44] Chen, S., Qiu, C., Yang, W., Zhang, Z.: Combining edge guidance and feature pyramid for medical image segmentation. *Biomedical signal processing and control* **78**, 103960 (2022)
- [45] Chen, S., Zhong, L., Qiu, C., Zhang, Z., Zhang, X.: Transformer-based multilevel region and edge aggregation network for magnetic resonance image segmentation. *Computers in Biology and Medicine* **152**, 106427 (2023)
- [46] Li, F., Li, W., Gao, X., Liu, R., Xiao, B.: Comprehensive information integration network for left atrium segmentation on lge cmr images. *Biomedical Signal Processing and Control* **81**, 104537 (2023)
- [47] Liu, Y., Dai, Y., Yan, C., Wang, K.: Deep learning based method for left atrial segmentation in ge-mri. In: Statistical Atlases and Computational Models of the Heart. Atrial Segmentation and LV Quantification Challenges: 9th International Workshop, STACOM 2018, Held in Conjunction with MICCAI 2018, Granada, Spain, September 16, 2018, Revised Selected Papers 9, pp. 311–318 (2019). Springer
- [48] Borra, D., Masci, A., Esposito, L., Andalò, A., Fabbri, C., Corsi, C.: A semantic-wise convolutional neural network approach for 3-d left atrium segmentation from late gadolinium enhanced magnetic resonance imaging. In: Statistical Atlases and Computational Models of the Heart. Atrial Segmentation and LV Quantification Challenges: 9th International Workshop, STACOM 2018, Held in Conjunction with MICCAI 2018, Granada, Spain, September 16, 2018, Revised Selected Papers 9, pp. 329–338 (2019). Springer
- [49] Puybureau, É., Zhao, Z., Khoudli, Y., Carlinet, E., Xu, Y., Lacotte, J., Géraud,

- T.: Left atrial segmentation in a few seconds using fully convolutional network and transfer learning. In: International Workshop on Statistical Atlases and Computational Models of the Heart, pp. 339–347 (2018). Springer
- [50] Uslu, F., Varela, M., Boniface, G., Mahenthiran, T., Chubb, H., Bharath, A.A.: La-net: A multi-task deep network for the segmentation of the left atrium. *IEEE transactions on medical imaging* **41**(2), 456–464 (2021)
- [51] Chen, J., Yang, G., Khan, H., Zhang, H., Zhang, Y., Zhao, S., Mohiaddin, R., Wong, T., Firmin, D., Keegan, J.: Jas-gan: generative adversarial network based joint atrium and scar segmentations on unbalanced atrial targets. *IEEE Journal of Biomedical and Health Informatics* **26**(1), 103–114 (2021)
- [52] Chen, S., Qiu, C., Yang, W., Zhang, Z.: Multiresolution aggregation transformer unet based on multiscale input and coordinate attention for medical image segmentation. *Sensors* **22**(10), 3820 (2022)
- [53] Qi, Y., Hu, C., Zuo, L., Yang, B., Lv, Y.: Cardiac magnetic resonance image segmentation method based on multi-scale feature fusion and sequence relationship learning. *Sensors* **23**(2), 690 (2023)
- [54] Zhao, C., Xiang, S., Wang, Y., Cai, Z., Shen, J., Zhou, S., Zhao, D., Su, W., Guo, S., Li, S.: Context-aware network fusing transformer and v-net for semi-supervised segmentation of 3d left atrium. *Expert Systems with Applications* **214**, 119105 (2023)
- [55] Milletari, F., Navab, N., Ahmadi, S.-A.: V-net: Fully convolutional neural networks for volumetric medical image segmentation. In: 2016 Fourth International Conference on 3D Vision (3DV), pp. 565–571 (2016). Ieee
- [56] Lourenço, A., Kerfoot, E., Dibblin, C., Alskaf, E., Anjari, M., Bharath, A.A., King, A.P., Chubb, H., Correia, T.M., Varela, M.: Left atrial ejection fraction estimation using seganet for fully automated segmentation of cine mri. In: Statistical Atlases and Computational Models of the Heart. M&Ms and EMIDEC Challenges: 11th International Workshop, STACOM 2020, Held in Conjunction with MICCAI 2020, Lima, Peru, October 4, 2020, Revised Selected Papers 11, pp. 137–145 (2021). Springer
- [57] Zhao, Z., Puybareau, E., Boutry, N., Géraud, T.: Do not treat boundaries and regions differently: An example on heart left atrial segmentation. In: 2020 25th International Conference on Pattern Recognition (ICPR), pp. 7447–7453 (2021). IEEE
- [58] Liu, Y., Wang, W., Luo, G., Wang, K., Liang, D., Li, S.: Uncertainty-guided symmetric multilevel supervision network for 3d left atrium segmentation in late gadolinium-enhanced mri. *Medical Physics* **49**(7), 4554–4565 (2022)

- [59] Guo, F., Ng, M., Roifman, I., Wright, G.: Cardiac mri left ventricular segmentation and function quantification using pre-trained neural networks. In: International Conference on Functional Imaging and Modeling of the Heart, pp. 46–54 (2021). Springer
- [60] Isensee, F., Jaeger, P.F., Full, P.M., Wolf, I., Engelhardt, S., Maier-Hein, K.H.: Automatic cardiac disease assessment on cine-mri via time-series segmentation and domain specific features. In: Statistical Atlases and Computational Models of the Heart. ACDC and MMWHS Challenges: 8th International Workshop, STACOM 2017, Held in Conjunction with MICCAI 2017, Quebec City, Canada, September 10-14, 2017, Revised Selected Papers 8, pp. 120–129 (2018). Springer
- [61] Simantiris, G., Tziritas, G.: Cardiac mri segmentation with a dilated cnn incorporating domain-specific constraints. *IEEE Journal of Selected Topics in Signal Processing* **14**(6), 1235–1243 (2020)
- [62] Berihu Girum, K., Créhange, G., Lalande, A.: Learning with context feedback loop for robust medical image segmentation. *arXiv e-prints*, 2103 (2021)
- [63] Ammar, A., Bouattane, O., Youssfi, M.: Automatic cardiac cine mri segmentation and heart disease classification. *Computerized Medical Imaging and Graphics* **88**, 101864 (2021)
- [64] Zotti, C., Luo, Z., Lalande, A., Jodoin, P.-M.: Convolutional neural network with shape prior applied to cardiac mri segmentation. *IEEE journal of biomedical and health informatics* **23**(3), 1119–1128 (2018)
- [65] Khened, M., Alex, V., Krishnamurthi, G.: Densely connected fully convolutional network for short-axis cardiac cine mr image segmentation and heart diagnosis using random forest. In: Statistical Atlases and Computational Models of the Heart. ACDC and MMWHS Challenges: 8th International Workshop, STACOM 2017, Held in Conjunction with MICCAI 2017, Quebec City, Canada, September 10-14, 2017, Revised Selected Papers 8, pp. 140–151 (2018). Springer
- [66] Baumgartner, C.F., Koch, L.M., Pollefeys, M., Konukoglu, E.: An exploration of 2d and 3d deep learning techniques for cardiac mr image segmentation. In: Statistical Atlases and Computational Models of the Heart. ACDC and MMWHS Challenges: 8th International Workshop, STACOM 2017, Held in Conjunction with MICCAI 2017, Quebec City, Canada, September 10-14, 2017, Revised Selected Papers 8, pp. 111–119 (2018). Springer
- [67] Painchaud, N., Skandarani, Y., Judge, T., Bernard, O., Lalande, A., Jodoin, P.-M.: Cardiac segmentation with strong anatomical guarantees. *IEEE transactions on medical imaging* **39**(11), 3703–3713 (2020)
- [68] Wolterink, J.M., Leiner, T., Viergever, M.A., Išgum, I.: Automatic segmentation and disease classification using cardiac cine mr images. In: Statistical Atlases

- and Computational Models of the Heart. ACDC and MMWHS Challenges: 8th International Workshop, STACOM 2017, Held in Conjunction with MICCAI 2017, Quebec City, Canada, September 10-14, 2017, Revised Selected Papers 8, pp. 101–110 (2018). Springer
- [69] Calisto, M.B., Lai-Yuen, S.K.: Adaen-net: An ensemble of adaptive 2d–3d fully convolutional networks for medical image segmentation. *Neural Networks* **126**, 76–94 (2020)
- [70] Zotti, C., Luo, Z., Humbert, O., Lalande, A., Jodoin, P.-M.: Gridnet with automatic shape prior registration for automatic mri cardiac segmentation. In: *Statistical Atlases and Computational Models of the Heart. ACDC and MMWHS Challenges: 8th International Workshop, STACOM 2017, Held in Conjunction with MICCAI 2017, Quebec City, Canada, September 10-14, 2017, Revised Selected Papers 8*, pp. 73–81 (2018). Springer
- [71] Singh, K.R., Sharma, A., Singh, G.K.: W-net: Novel deep supervision for deep learning-based cardiac magnetic resonance imaging segmentation. *IETE Journal of Research* **69**(12), 8960–8976 (2023)
- [72] Full, P.M., Isensee, F., Jäger, P.F., Maier-Hein, K.: Studying robustness of semantic segmentation under domain shift in cardiac mri. In: *Statistical Atlases and Computational Models of the Heart. M&Ms and EMIDEC Challenges: 11th International Workshop, STACOM 2020, Held in Conjunction with MICCAI 2020, Lima, Peru, October 4, 2020, Revised Selected Papers 11*, pp. 238–249 (2021). Springer
- [73] Parreño, M., Paredes, R., Albiol, A.: Deidentifying mri data domain by iterative backpropagation. In: *Statistical Atlases and Computational Models of the Heart. M&Ms and EMIDEC Challenges: 11th International Workshop, STACOM 2020, Held in Conjunction with MICCAI 2020, Lima, Peru, October 4, 2020, Revised Selected Papers 11*, pp. 277–286 (2021). Springer
- [74] Zhang, Y., Yang, J., Hou, F., Liu, Y., Wang, Y., Tian, J., Zhong, C., Zhang, Y., He, Z.: Semi-supervised cardiac image segmentation via label propagation and style transfer. In: *Statistical Atlases and Computational Models of the Heart. M&Ms and EMIDEC Challenges: 11th International Workshop, STACOM 2020, Held in Conjunction with MICCAI 2020, Lima, Peru, October 4, 2020, Revised Selected Papers 11*, pp. 219–227 (2021). Springer
- [75] Ma, J.: Histogram matching augmentation for domain adaptation with application to multi-centre, multi-vendor and multi-disease cardiac image segmentation. In: *Statistical Atlases and Computational Models of the Heart. M&Ms and EMIDEC Challenges: 11th International Workshop, STACOM 2020, Held in Conjunction with MICCAI 2020, Lima, Peru, October 4, 2020, Revised Selected Papers 11*, pp. 177–186 (2021). Springer

- [76] Saber, M., Abdelraouf, D., Elattar, M.: Multi-center, multi-vendor, and multi-disease cardiac image segmentation using scale-independent multi-gate unet. In: *Statistical Atlases and Computational Models of the Heart. M&Ms and EMIDEC Challenges: 11th International Workshop, STACOM 2020, Held in Conjunction with MICCAI 2020, Lima, Peru, October 4, 2020, Revised Selected Papers 11*, pp. 259–268 (2021). Springer
- [77] Kong, F., Shadden, S.C.: A generalizable deep-learning approach for cardiac magnetic resonance image segmentation using image augmentation and attention u-net. In: *Statistical Atlases and Computational Models of the Heart. M&Ms and EMIDEC Challenges: 11th International Workshop, STACOM 2020, Held in Conjunction with MICCAI 2020, Lima, Peru, October 4, 2020, Revised Selected Papers 11*, pp. 287–296 (2021). Springer
- [78] Corral Acero, J., Sundaresan, V., Dinsdale, N., Grau, V., Jenkinson, M.: A 2-step deep learning method with domain adaptation for multi-centre, multi-vendor and multi-disease cardiac magnetic resonance segmentation. In: *Statistical Atlases and Computational Models of the Heart. M&Ms and EMIDEC Challenges: 11th International Workshop, STACOM 2020, Held in Conjunction with MICCAI 2020, Lima, Peru, October 4, 2020, Revised Selected Papers 11*, pp. 196–207 (2021). Springer
- [79] Li, H., Zhang, J., Menze, B.: Generalisable cardiac structure segmentation via attentional and stacked image adaptation. In: *Statistical Atlases and Computational Models of the Heart. M&Ms and EMIDEC Challenges: 11th International Workshop, STACOM 2020, Held in Conjunction with MICCAI 2020, Lima, Peru, October 4, 2020, Revised Selected Papers 11*, pp. 297–304 (2021). Springer
- [80] Khader, F., Schock, J., Truhn, D., Morsbach, F., Haarbuerger, C.: Adaptive pre-processing for generalization in cardiac mr image segmentation. In: *Statistical Atlases and Computational Models of the Heart. M&Ms and EMIDEC Challenges: 11th International Workshop, STACOM 2020, Held in Conjunction with MICCAI 2020, Lima, Peru, October 4, 2020, Revised Selected Papers 11*, pp. 269–276 (2021). Springer
- [81] Carscadden, A., Noga, M., Punithakumar, K.: A deep convolutional neural network approach for the segmentation of cardiac structures from mri sequences. In: *Statistical Atlases and Computational Models of the Heart. M&Ms and EMIDEC Challenges: 11th International Workshop, STACOM 2020, Held in Conjunction with MICCAI 2020, Lima, Peru, October 4, 2020, Revised Selected Papers 11*, pp. 250–258 (2021). Springer
- [82] Scannell, C.M., Chiribiri, A., Veta, M.: Domain-adversarial learning for multi-centre, multi-vendor, and multi-disease cardiac mr image segmentation. In: *Statistical Atlases and Computational Models of the Heart. M&Ms and EMIDEC Challenges: 11th International Workshop, STACOM 2020, Held in Conjunction*

- with MICCAI 2020, Lima, Peru, October 4, 2020, Revised Selected Papers 11, pp. 228–237 (2021). Springer
- [83] Huang, X., Chen, Z., Yang, X., Liu, Z., Zou, Y., Luo, M., Xue, W., Ni, D.: Style-invariant cardiac image segmentation with test-time augmentation. In: Statistical Atlases and Computational Models of the Heart. M&Ms and EMIDEC Challenges: 11th International Workshop, STACOM 2020, Held in Conjunction with MICCAI 2020, Lima, Peru, October 4, 2020, Revised Selected Papers 11, pp. 305–315 (2021). Springer
- [84] Liu, X., Thermos, S., Chartsias, A., O’Neil, A., Tsaftaris, S.A.: Disentangled representations for domain-generalized cardiac segmentation. In: Statistical Atlases and Computational Models of the Heart. M&Ms and EMIDEC Challenges: 11th International Workshop, STACOM 2020, Held in Conjunction with MICCAI 2020, Lima, Peru, October 4, 2020, Revised Selected Papers 11, pp. 187–195 (2021). Springer
- [85] Li, L., Zimmer, V.A., Ding, W., Wu, F., Huang, L., Schnabel, J.A., Zhuang, X.: Random style transfer based domain generalization networks integrating shape and spatial information. In: Statistical Atlases and Computational Models of the Heart. M&Ms and EMIDEC Challenges: 11th International Workshop, STACOM 2020, Held in Conjunction with MICCAI 2020, Lima, Peru, October 4, 2020, Revised Selected Papers 11, pp. 208–218 (2021). Springer
- [86] Fulton, M.J., Heckman, C.R., Rentschler, M.E.: Deformable bayesian convolutional networks for disease-robust cardiac mri segmentation. In: International Workshop on Statistical Atlases and Computational Models of the Heart, pp. 296–305 (2021). Springer
- [87] Arega, T.W., Legrand, F., Bricq, S., Meriaudeau, F.: Using mri-specific data augmentation to enhance the segmentation of right ventricle in multi-disease, multi-center and multi-view cardiac mri. In: International Workshop on Statistical Atlases and Computational Models of the Heart, pp. 250–258 (2021). Springer
- [88] Punithakumar, K., Carscadden, A., Noga, M.: Automated segmentation of the right ventricle from magnetic resonance imaging using deep convolutional neural networks. In: International Workshop on Statistical Atlases and Computational Models of the Heart, pp. 344–351 (2021). Springer
- [89] Li, L., Ding, W., Huang, L., Zhuang, X.: Right ventricular segmentation from short-and long-axis mris via information transition. In: International Workshop on Statistical Atlases and Computational Models of the Heart, pp. 259–267 (2021). Springer
- [90] Sun, X., Cheng, L.-H., Geest, R.J.: Right ventricle segmentation via registration

- and multi-input modalities in cardiac magnetic resonance imaging from multi-disease, multi-view and multi-center. In: *Statistical Atlases and Computational Models of the Heart. Multi-Disease, Multi-View, and Multi-Center Right Ventricular Segmentation in Cardiac MRI Challenge: 12th International Workshop, STACOM 2021, Held in Conjunction with MICCAI 2021, Strasbourg, France, September 27, 2021, Revised Selected Papers 12*, pp. 241–249 (2022). Springer
- [91] Al Khalil, Y., Amirrajab, S., Pluim, J., Breeuwer, M.: Late fusion u-net with gan-based augmentation for generalizable cardiac mri segmentation. In: *International Workshop on Statistical Atlases and Computational Models of the Heart*, pp. 360–373 (2021). Springer
- [92] Liu, D., Yan, Z., Chang, Q., Axel, L., Metaxas, D.N.: Refined deep layer aggregation for multi-disease, multi-view & multi-center cardiac mr segmentation. In: *International Workshop on Statistical Atlases and Computational Models of the Heart*, pp. 315–322 (2021). Springer
- [93] Jabbar, S., Bukhari, S.T., Mohy-ud-Din, H.: Multi-view sa-la net: A framework for simultaneous segmentation of rv on multi-view cardiac mr images. In: *International Workshop on Statistical Atlases and Computational Models of the Heart*, pp. 277–286 (2021). Springer
- [94] Queirós, S.: Right ventricular segmentation in multi-view cardiac mri using a unified u-net model. In: *International Workshop on Statistical Atlases and Computational Models of the Heart*, pp. 287–295 (2021). Springer
- [95] Galati, F., Zuluaga, M.A.: Using out-of-distribution detection for model refinement in cardiac image segmentation. In: *International Workshop on Statistical Atlases and Computational Models of the Heart*, pp. 374–382 (2021). Springer
- [96] Mazher, M., Qayyum, A., Benzinou, A., Abdel-Nasser, M., Puig, D.: Multi-disease, multi-view and multi-center right ventricular segmentation in cardiac mri using efficient late-ensemble deep learning approach. In: *International Workshop on Statistical Atlases and Computational Models of the Heart*, pp. 335–343 (2021). Springer
- [97] Gao, Z., Zhuang, X.: Consistency based co-segmentation for multi-view cardiac mri using vision transformer. In: *Statistical Atlases and Computational Models of the Heart. Multi-Disease, Multi-View, and Multi-Center Right Ventricular Segmentation in Cardiac MRI Challenge: 12th International Workshop, STACOM 2021, Held in Conjunction with MICCAI 2021, Strasbourg, France, September 27, 2021, Revised Selected Papers 12*, pp. 306–314 (2022). Springer
- [98] Beetz, M., Corral Acero, J., Grau, V.: A multi-view crossover attention u-net cascade with fourier domain adaptation for multi-domain cardiac mri segmentation. In: *International Workshop on Statistical Atlases and Computational Models of the Heart*, pp. 323–334 (2021). Springer

- [99] Tautz, L., Walczak, L., Manini, C., Hennemuth, A., Hüllebrand, M.: 3d right ventricle reconstruction from 2d u-net segmentation of sparse short-axis and 4-chamber cardiac cine mri views. In: International Workshop on Statistical Atlases and Computational Models of the Heart, pp. 352–359 (2021). Springer
- [100] Galazis, C., Wu, H., Li, Z., Petri, C., Bharath, A.A., Varela, M.: Tempera: Spatial transformer feature pyramid network for cardiac mri segmentation. In: International Workshop on Statistical Atlases and Computational Models of the Heart, pp. 268–276 (2021). Springer

Additional file 1

A1 Evaluation Metrics

Here we explained the evaluation metrics in detail.

A1.0.1 Dice Score

The Dice Similarity Coefficient (DSC) is a measure of overlap between the predicted segmentation and the ground truth, calculated as twice the area of overlap divided by the total number of pixels in both the predicted and ground truth masks. A higher DSC indicates better performance, signifying a greater degree of similarity between the predicted and actual segmentation.

$$DSC = \frac{2 \cdot |P \cap Q|}{|P| + |Q|} \quad (\text{A1.1})$$

where P and Q are the ground truth and predicted masks.

A1.0.2 Jaccard Index

The Jaccard Index, also known as the Intersection over Union (IoU), quantifies the similarity between the predicted and ground truth segmentation. It is defined as the area of overlap divided by the area of the union of the predicted and ground truth masks. Similar to the DSC, a higher Jaccard Index denotes better segmentation performance.

$$Jaccard = \frac{|P \cap Q|}{|P \cup Q|} \quad (\text{A1.2})$$

where P and Q are the ground truth and predicted masks.

A1.0.3 Hausdorff Distance

The Hausdorff Distance (HD) measures the maximum distance from a point in the predicted segmentation to the nearest point in the ground truth segmentation, thus indicating the worst-case boundary discrepancy. Lower HD values indicate more accurate boundary delineation.

$$HD(P, Q) = \max(h(P, Q), h(Q, P)) \quad (\text{A1.3})$$

where $h(P, Q)$ is the oriented Hausdorff distance from P to Q :

$$h(P, Q) = \max_{p_i \in P} \min_{q_j \in Q} \rho(p_i, q_j) \quad (\text{A1.4})$$

and $\rho(p_i, q_j)$ is the Euclidean distance between points p_i and q_j .

A1.0.4 Mean Surface Distance

The Mean Surface Distance (MSD) calculates the average distance between points on the surface of the predicted segmentation and the nearest points on the surface of

the ground truth segmentation. Lower MSD values suggest closer average alignment between the predicted and actual boundaries.

$$MSD(P, Q) = \frac{1}{|P|} \sum_{p_i \in P} \min_{q_j \in Q} \rho(p_i, q_j) \quad (\text{A1.5})$$

A1.0.5 95th percentile Hausdorff Distance

The 95th percentile Hausdorff Distance (HD95) is similar to the HD but focuses on the 95th percentile of the distances between the predicted and ground truth surfaces, thereby mitigating the impact of outliers. A lower HD95 value indicates more consistent boundary accuracy, discounting extreme deviations.

Together, these metrics provide a robust framework for evaluating segmentation performance, with higher DSC and Jaccard Index values and lower HD, MSD, and HD95 values indicating superior model performance.

A2 Datasets

A summary of the datasets is shown in Table A1.

Table A1: Summary of Cardiac MRI Datasets

Dataset	Task	Labels	Training	Testing
LAScarQS	Task 1	LA cavity, scars	50	10
	Task 2	LA cavity	130	20
LASC	-	LA cavity	100	54
ACDC	End-Diastole	LV, MYO, RV	100	50
	End-Systole		100	50
MnM-1	End-Diastole	LV, MYO, RV	150	136
	End-Systole		150	136
MnM-2	Short Axis, End-Diastole	LV, MYO, RV	200	160
	Short Axis, End-Systole		200	160
	Long Axis, End-Diastole		200	160
	Long Axis, End-Systole		200	160

A3 Additional Results

A3.1 Validation set and test set results

In Tables A2 and A3, we present the performance results for the validation and test sets, reported as mean \pm standard deviation. For the validation set, the results are averaged across the five folds, whereas for the test set, the averages are computed over all test images.

Table A2: Validation set performance comparison across LAScarQS, LASC, ACDC, MnM, and MnM2 datasets, reported as mean \pm std. Abbreviations: Config. Configuration, LAC - Left Atrial Cavity, RV - Right Ventricle, MYO - Myocardium, LV - Left Ventricle, ED - End Diastole, ES - End Systole, full - full resolution, low - low resolution, cas. - cascade.

Dataset	Task	Config.	Label	Dice	HD95
LAScarQS	Task2	2D	LAC	0.921 ± 0.0080	3.866 ± 0.4962
		3D full.	LAC	0.925 ± 0.0071	3.707 ± 0.3914
		3D low.	LAC	0.927 ± 0.0057	3.454 ± 0.2390
		3D cas.	LAC	0.926 ± 0.0054	3.621 ± 0.3089
	Task1	2D	LAC	0.900 ± 0.0244	4.427 ± 0.6797
			Scar	0.493 ± 0.0524	7.942 ± 1.6955
		3D full.	LAC	0.923 ± 0.0131	3.334 ± 0.3076
			Scar	0.501 ± 0.0452	7.898 ± 1.7594
		3D low.	LAC	0.923 ± 0.0116	3.346 ± 0.4136
			Scar	0.474 ± 0.0496	8.554 ± 1.6419
3D cas.	LAC	0.923 ± 0.0093	3.612 ± 0.4662		
	Scar	0.472 ± 0.1110	8.662 ± 3.0562		
LASC	-	2D	LAC	0.909 ± 0.0199	4.830 ± 0.8469
		3D full.	LAC	0.927 ± 0.0036	4.079 ± 0.2672
		3D low.	LAC	0.926 ± 0.0043	3.984 ± 0.3186
		3D cas.	LAC	0.927 ± 0.0041	4.032 ± 0.3590
ACDC	ED	2D	RV	0.935 ± 0.0053	3.461 ± 0.6634
			MYO	0.894 ± 0.0092	1.693 ± 0.2132
			LV	0.964 ± 0.0029	2.454 ± 0.7448
		3D full.	RV	0.935 ± 0.0053	3.461 ± 0.6634
	MYO	0.894 ± 0.0092	1.693 ± 0.2132		
	LV	0.964 ± 0.0029	2.454 ± 0.7448		
	ES	2D	RV	0.871 ± 0.0167	5.110 ± 1.0900
			MYO	0.904 ± 0.0048	2.244 ± 0.3354
LV			0.923 ± 0.0111	4.487 ± 1.1083	
3D full.		RV	0.852 ± 0.0113	6.053 ± 0.4896	
MYO	0.901 ± 0.0080	2.348 ± 0.4481			
LV	0.924 ± 0.0139	3.137 ± 0.5750			
MnM	ED	2D	LV	0.947 ± 0.0194	3.658 ± 1.2410
			MYO	0.861 ± 0.0267	3.666 ± 1.6247
			RV	0.919 ± 0.0110	4.304 ± 1.0132
	3D full.	LV	0.950 ± 0.0041	3.285 ± 0.3301	
		MYO	0.861 ± 0.0105	3.041 ± 0.5260	
		RV	0.908 ± 0.0114	5.116 ± 0.9079	

Table A2: (continued)

Dataset	Task	Config.	Label	Dice	HD95	
	ES	2D	LV	0.903 ± 0.0108	4.442 ± 0.8087	
			MYO	0.872 ± 0.0165	3.290 ± 0.9736	
			RV	0.863 ± 0.0208	4.844 ± 0.5368	
		3D full.	LV	0.902 ± 0.0078	4.055 ± 0.3486	
			MYO	0.867 ± 0.0098	3.323 ± 0.4579	
			RV	0.851 ± 0.0170	5.629 ± 1.0387	
MnM2	LA ED	3D full.	LV	0.969 ± 0.0032	2.597 ± 0.2565	
			MYO	0.872 ± 0.0101	1.937 ± 0.2253	
			RV	0.936 ± 0.0065	4.355 ± 1.0182	
	LA ES	3D full.	LV	0.956 ± 0.0066	2.780 ± 0.3659	
			MYO	0.895 ± 0.0122	2.190 ± 0.3762	
			RV	0.909 ± 0.0161	4.207 ± 1.2462	
	SA ED	2D	LV	0.958 ± 0.0032	3.672 ± 0.6647	
			MYO	0.872 ± 0.0056	2.761 ± 0.3829	
			RV	0.940 ± 0.0086	3.961 ± 1.1052	
			3D full.	LV	0.961 ± 0.0029	3.163 ± 0.3944
				MYO	0.872 ± 0.0076	2.427 ± 0.3216
				RV	0.935 ± 0.0081	4.780 ± 1.1574
SA ES	2D	LV	0.958 ± 0.0025	3.804 ± 0.6177		
		MYO	0.870 ± 0.0081	2.913 ± 0.2344		
		RV	0.943 ± 0.0099	3.426 ± 0.9041		
	3D full.	LV	0.957 ± 0.0025	3.563 ± 0.2242		
		MYO	0.871 ± 0.0100	2.580 ± 0.3922		
		RV	0.939 ± 0.0084	4.038 ± 1.0009		

Table A3: Test set performance comparison across LAScarQS, LASC, ACDC, MnM, and MnM2 datasets, reported as mean \pm std. Abbreviations: Config. Configuration, LAC - Left Atrial Cavity, RV - Right Ventricle, MYO - Myocardium, LV - Left Ventricle, ED - End Diastole, ES - End Systole, full - full resolution, low - low resolution, cas. - cascade, Ens.- Ensemble.

Dataset	Task	Config.	Label	Dice	HD95
LAScarQS	Task2	2D	LAC	0.930 ± 0.0168	3.017 ± 0.9052
		3D full.	LAC	0.937 ± 0.0149	2.880 ± 0.9661
		3D low.	LAC	0.935 ± 0.0164	3.069 ± 1.3614
		3D cas.	LAC	0.937 ± 0.0161	2.745 ± 0.8492
		Ens.	LAC	0.938 ± 0.0151	2.737 ± 0.8157

Table A3: (continued)

Dataset	Task	Config.	Label	Dice	HD95
	Task1	2D	LAC	0.926 ± 0.0151	3.402 ± 1.1058
			Scar	0.438 ± 0.0755	13.036 ± 5.7312
		3D full.	LAC	0.939 ± 0.0099	3.088 ± 1.0105
			Scar	0.443 ± 0.0911	12.620 ± 3.6403
		3D low.	LAC	0.937 ± 0.0126	3.254 ± 1.2967
Scar	0.411 ± 0.0841		13.425 ± 3.5387		
LASC	-	3D cas.	LAC	0.939 ± 0.0096	3.138 ± 1.1646
			Scar	0.449 ± 0.0852	12.554 ± 3.6200
		Ens.	LAC	0.939 ± 0.0105	3.041 ± 1.0385
			Scar	0.439 ± 0.0878	12.850 ± 3.6996
			2D	LAC	0.926 ± 0.0227
ACDC	ED	3D full.	LAC	0.933 ± 0.0202	3.681 ± 2.0243
			LAC	0.931 ± 0.0214	3.727 ± 2.0254
		3D cas.	LAC	0.933 ± 0.0210	3.756 ± 2.0699
			LAC	0.934 ± 0.0204	3.628 ± 2.0353
		Ens.	LAC	0.934 ± 0.0204	3.628 ± 2.0353
2D	RV		0.942 ± 0.0361	3.152 ± 2.7885	
	MYO		0.897 ± 0.0197	1.583 ± 0.2452	
	LV	0.965 ± 0.0170	2.350 ± 2.2734		
		3D full.	RV	0.934 ± 0.0469	3.861 ± 4.0508
			MYO	0.889 ± 0.0218	2.135 ± 1.9664
			LV	0.959 ± 0.0258	2.720 ± 2.6258
		Ens.	RV	0.944 ± 0.0367	3.110 ± 2.8565
			MYO	0.898 ± 0.0194	1.818 ± 1.4122
			LV	0.963 ± 0.0212	2.474 ± 2.3381
	ES	2D	RV	0.885 ± 0.0578	4.318 ± 3.7865
			MYO	0.913 ± 0.0245	1.975 ± 1.4111
			LV	0.927 ± 0.0496	2.713 ± 2.6216
		3D full.	RV	0.882 ± 0.0591	5.245 ± 3.7910
			MYO	0.906 ± 0.0239	2.551 ± 2.4158
		Ens.	LV	0.901 ± 0.0884	4.968 ± 6.0382
			RV	0.892 ± 0.0555	4.208 ± 3.8025
			MYO	0.915 ± 0.0211	2.193 ± 1.9121
MnM	ED	2D	LV	0.922 ± 0.0601	3.477 ± 3.3692
			MYO	0.936 ± 0.0752	3.871 ± 5.5988
			RV	0.824 ± 0.0537	3.676 ± 5.1438
		3D full.	RV	0.909 ± 0.0823	4.578 ± 5.0231
			LV	0.933 ± 0.0678	4.261 ± 3.4927

Table A3: (continued)

Dataset	Task	Config.	Label	Dice	HD95	
MnM2			MYO	0.819 ± 0.0451	3.484 ± 3.1505	
			RV	0.908 ± 0.0906	4.501 ± 5.3539	
			Ens.	LV	0.937 ± 0.0530	3.761 ± 4.1780
				MYO	0.826 ± 0.0645	3.138 ± 3.3104
				RV	0.913 ± 0.0865	4.208 ± 4.5919
	ES	2D	LV	0.888 ± 0.0380	8.513 ± 3.6098	
			MYO	0.800 ± 0.0648	7.304 ± 4.6097	
			RV	0.893 ± 0.0526	6.411 ± 3.8556	
		3D full.	LV	0.909 ± 0.0429	4.507 ± 4.0052	
			MYO	0.841 ± 0.0651	3.952 ± 3.1857	
			RV	0.871 ± 0.0515	5.673 ± 3.7000	
		Ens.	LV	0.888 ± 0.0405	4.432 ± 3.2381	
			MYO	0.864 ± 0.0486	3.542 ± 3.4477	
			RV	0.852 ± 0.0884	5.366 ± 3.7532	
		LA ED	3D full.	LV	0.968 ± 0.0216	2.977 ± 2.2622
			MYO	0.878 ± 0.0571	2.151 ± 1.6604	
			RV	0.934 ± 0.0302	4.075 ± 2.2530	
	LA ES	3D full.	LV	0.948 ± 0.0376	3.246 ± 3.1302	
			MYO	0.891 ± 0.0666	2.809 ± 4.2584	
			RV	0.899 ± 0.0656	4.254 ± 3.4218	
	SA ED	2D	LV	0.957 ± 0.0272	3.169 ± 3.4790	
			MYO	0.867 ± 0.0546	2.842 ± 3.5519	
			RV	0.934 ± 0.0415	4.083 ± 3.8421	
		3D full.	LV	0.955 ± 0.0252	3.571 ± 3.5109	
			MYO	0.862 ± 0.0525	2.561 ± 2.4932	
			RV	0.934 ± 0.0403	4.200 ± 3.8857	
		Ens.	LV	0.958 ± 0.0253	3.256 ± 3.4665	
			MYO	0.869 ± 0.0518	2.371 ± 2.4556	
			RV	0.937 ± 0.0394	4.021 ± 4.1842	
	SA ES	2D	LV	0.958 ± 0.0272	3.170 ± 3.4631	
			MYO	0.867 ± 0.0543	2.571 ± 2.8774	
			RV	0.934 ± 0.0425	4.520 ± 6.4278	
		3D full.	LV	0.956 ± 0.0252	3.481 ± 3.4478	
			MYO	0.862 ± 0.0521	2.555 ± 2.4800	
			RV	0.934 ± 0.0414	4.302 ± 4.0415	
		Ens.	LV	0.958 ± 0.0255	3.264 ± 3.4861	
			MYO	0.868 ± 0.0516	2.341 ± 2.4096	

Table A3: (continued)

Dataset	Task	Config.	Label	Dice	HD95
			RV	0.938 ± 0.0380	3.929 ± 4.0974

A3.2 Comparison with other models

A3.2.1 LAScarQS

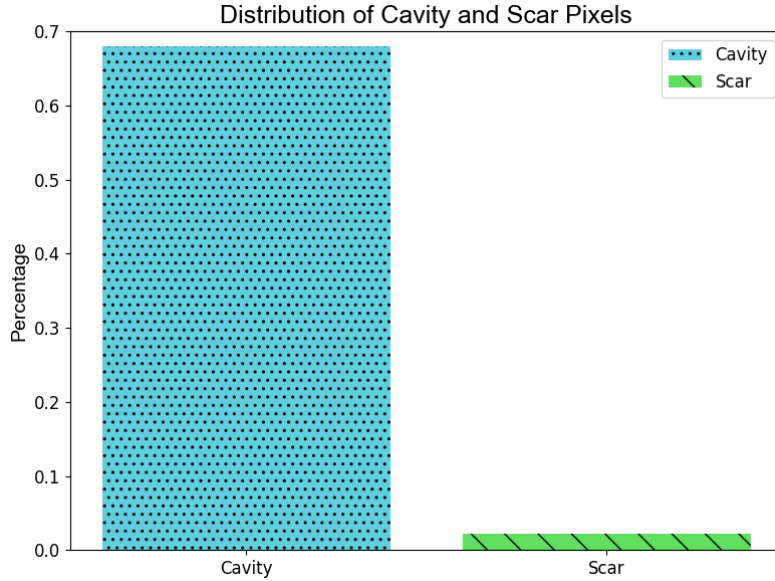


Fig. A1: Total pixel distribution of 60 images of LAScarQS Task1.

In Fig. A1 shows the pixel distribution of the cavity and scar for 60 MRIs from the LAScarQS Task 1. While most of the area belongs to the background, nearly 0.7% pixels are cavity and less than 0.1% belongs to the scar region. This showcases the class imbalance nature of the scar and cavity pixels.

In Table A4 we compare the results of the nnU-Net with other models which used the same dataset for Task1 using dice scores. Table A4 shows the performance of the Task 2 with nnUNet and other models with DSC, HD and MSD matrices.

A3.2.2 LASC

In Table A6, the performance of the nnU-Net and other models are compared using DSC values.

Table A4: Performance comparison of dice scores in nnU-Net variations and other models in LAScarQS-Task1 for scar and cavity segmentation.

Method	Scars	Cavity
Punithakumar et al. (2022)[?]	0.660	0.907
Jiang et al. (2022)[15]	0.641	0.902
Arega et al. (2022)[12]	0.634	0.898
Mazher et al. (2022)[14]	0.602	0.875
Zhang et al. (2022)[30]	0.598	0.880
Lefebvre et al. (2022)[31]	0.553	0.938
nnU-Net (2D)	0.439	0.926
nnU-Net (3D full resolution)	0.443	0.939
nnU-Net (3D low resolution)	0.411	0.937
nnU-Net (3D cascade)	0.449	0.939
nnU-Net (Ensemble)	0.439	0.939

Table A5: Performance comparison of nnU-Net variations and other models in LAScarQS-Task2. DSC- Dice Score, HD - Hausdorff Distance, MSD- Mean Surface Distance

Method	DSC	HD	MSD
Lefebvre et al. (2022)[31]	0.889	26.270	2.179
Tu et al. (2022)[32]	0.890	17.124	1.706
Liu et al. (2022)[33]	0.866	-	-
Zhang et al. (2022)[30]	0.890	16.450	1.715
Zhang et al. (2022)[34]	0.878	-	0.710
Khan et al. (2022)[35]	0.846	105.700	3.390
Xie et al. (2022)[36]	0.872	22.394	-
Zhou et al. (2022)[37]	0.875	24.731	2.233
Jiang et al. (2022)[15]	0.881	18.755	1.782
Li et al. (2022)[38]	0.883	20.883	1.794
Arega et al. (2022)[12]	0.890	16.907	1.720
Punithakumar et al. (2022)[?]	0.893	15.860	1.613
Mazher et al. (2022)[14]	0.886	18.389	1.813
Singh et al. (2023)[24]	0.929	12.960	0.890
Singh et al. (2023)[39]	0.919	15.430	-
nnU-Net (2D)	0.930	13.971	0.733
nnU-Net (3D full resolution)	0.937	12.971	0.672
nnU-Net (3D low resolution)	0.935	12.741	0.692
nnU-Net (3D cascade)	0.937	12.807	0.667
nnU-Net (Ensemble)	0.938	12.767	0.652

A3.2.3 ACDC

In Table A7, the performance of the nnU-Net and other models are compared using DSC and HD values for both End Diastole (ED) and End Systole (ES) phases for Left Ventricles (LV), Myocardium (MYO) and Right Ventricles (RV).

Table A6: Performance comparison of nnU-Net variations and other models in LASC. DSC- Dice Score

Publication	DSC
Xia et al. (2019)[40]	0.932
Bian et al. (2018)[41]	0.926
Vesal et al. (2019)[42]	0.925
Yang et al. (2019)[11]	0.925
Li et al. (2019)[43]	0.923
Chen et al. (2022)[44]	0.920
Chen et al. (2023)[45]	0.932
Li et al. (2023)[46]	0.919
Liu et al. (2019)[47]	0.903
Borra et al. (2019)[48]	0.898
Puybureau et al. (2018)[49]	0.923
Uslu et al. (2021)[50]	0.920
Chen et al. (2021)[51]	0.913
Chen et al. (2022)[52]	0.923
Qi et al. (2023)[53]	0.921
Zhao et al. (2023)[54]	0.911
Singh et al. (2023)[24]	0.935
Singh et al. (2023)[39]	0.934
Milletari et al. (2016)[55]	0.919
Lourenço et al. (2021)[56]	0.910
Zhao et al. (2021)[57]	0.918
Liu et al. (2022)[58]	0.920
Xu et al. (2024)[25]	0.926
nnU-Net (2D)	0.926
nnU-Net (3D full resolution)	0.933
nnU-Net (3D low resolution)	0.931
nnU-Net (3D cascade)	0.933
nnU-Net (Ensemble)	0.934

A3.2.4 MnM

In Table A8, the performance of the nnU-Net and other models are compared using DSC and HD values for both ED and ES phases for LV, MYO and RV.

A3.2.5 MnM2

In Table A9, the performance of the nnU-Net and other models are compared using DSC and HD values for both ED and ES phases for RV only for both short and long axis.

Table A7: Performance comparison of nnU-Net variations and other models in ACDC. LV- Left Ventricle, MYO- Myocardium, RV- Right Ventricle, ED- End Diastole, ES - End Systole, DSC- Dice Score, HD - Hausdorff Distance.

Method	LV						MYO						RV					
	ED		ES		HD		ED		ES		HD		ED		ES		HD	
	DSC	HD	DSC	HD	DSC	HD	DSC	HD	DSC	HD	DSC	HD	DSC	HD	DSC	HD	DSC	HD
Guo et al. (2021)[59]	0.968	5.814	0.935	7.361	0.906	7.469	0.923	7.702	0.955	8.877	0.894	11.649						
Isensee et al. (2018)[60]	0.967	5.476	0.928	6.921	0.904	7.014	0.923	7.328	0.951	8.205	0.904	11.665						
Simantiris et al. (2020)[61]	0.967	6.366	0.928	7.573	0.891	8.264	0.904	9.575	0.936	13.289	0.889	14.367						
Berihu et al. (2021)[62]	0.968	6.422	0.916	9.305	0.894	8.998	0.906	9.922	0.939	11.326	0.893	13.306						
Ammar et al. (2021)[63]	0.968	7.993	0.911	10.528	0.891	10.575	0.901	13.891	0.929	14.189	0.886	16.042						
Zotti et al. (2018)[64]	0.964	6.180	0.912	8.386	0.886	9.586	0.902	9.291	0.934	11.052	0.885	12.650						
Khened et al. (2018)[65]	0.964	8.129	0.917	8.968	0.889	9.841	0.898	12.582	0.935	13.994	0.879	13.930						
Baumgartner et al. (2018)[66]	0.963	6.526	0.911	9.170	0.892	8.703	0.901	10.637	0.932	12.670	0.883	14.691						
Painchaud et al. (2020)[67]	0.961	6.152	0.911	8.278	0.881	8.651	0.897	9.598	0.933	13.718	0.884	13.323						
Wolterink et al. (2018)[68]	0.961	7.515	0.918	6.603	0.875	11.121	0.894	10.687	0.928	11.879	0.872	13.399						
Calisto et al. (2020)[69]	0.958	5.592	0.903	8.644	0.873	8.197	0.895	8.318	0.936	10.183	0.884	12.234						
Zotti et al. (2018)[70]	0.957	6.641	0.905	8.706	0.884	8.708	0.896	9.264	0.941	10.318	0.882	14.053						
Singh et al. (2023)[71]	0.967	5.526	0.935	6.913	0.902	8.094	0.921	7.772	0.949	9.187	0.900	11.556						
Singh et al. (2023)[24]	0.967	5.652	0.938	6.878	0.905	7.389	0.923	7.373	0.950	8.513	0.895	12.167						
Singh et al. (2023)[39]	0.968	5.859	0.937	6.529	0.904	7.723	0.922	7.221	0.952	8.788	0.890	11.926						
nnU (2D)	0.965	6.739	0.927	6.795	0.897	10.050	0.913	8.231	0.942	10.438	0.885	12.678						
nnU (3D full resolution)	0.959	8.486	0.901	9.028	0.889	8.057	0.906	8.785	0.934	11.494	0.882	12.743						
nnU (Ensemble)	0.963	9.584	0.922	8.321	0.898	9.884	0.915	8.460	0.944	10.716	0.892	12.200						

Table A8: Performance comparison of nnU-Net variations and other models in MnM. LV- Left Ventricle, MYO- Myocardium, RV- Right Ventricle, ED- End Dystole, ES - End Systole, DSC- Dice Score, HD - Hausdorff Distance.

Method	LV						MYO						RV											
	ED		DSC		ES		ED		DSC		ES		ED		DSC		ES							
	DSC	HD	DSC	HD	DSC	HD	DSC	HD	DSC	HD	DSC	HD	DSC	HD	DSC	HD	DSC	HD						
Full et al. (2021)[72]	0.939	9.1	0.886	9.1	0.839	12.8	0.867	10.6	0.910	11.8	0.860	12.7	0.939	9.1	0.886	9.1	0.839	12.8	0.867	10.6	0.910	11.8	0.860	12.7
Parreno et al. (2021)[73]	0.939	11.3	0.884	11.4	0.826	15.2	0.856	14.0	0.886	15.4	0.829	16.7	0.939	11.3	0.884	11.4	0.826	15.2	0.856	14.0	0.886	15.4	0.829	16.7
Zhang et al. (2021)[74]	0.938	9.3	0.880	9.5	0.830	12.9	0.861	10.8	0.909	12.3	0.850	13.0	0.938	9.3	0.880	9.5	0.830	12.9	0.861	10.8	0.909	12.3	0.850	13.0
Ma et al. (2021)[75]	0.935	9.5	0.875	10.5	0.825	13.3	0.856	11.6	0.906	12.3	0.844	13.0	0.935	9.5	0.875	10.5	0.825	13.3	0.856	11.6	0.906	12.3	0.844	13.0
Saber et al. (2021)[76]	0.933	13.4	0.867	14.0	0.812	17.1	0.839	18.2	0.876	15.7	0.815	18.1	0.933	13.4	0.867	14.0	0.812	17.1	0.839	18.2	0.876	15.7	0.815	18.1
Kong et al. (2021)[77]	0.931	10.0	0.877	9.8	0.816	13.7	0.850	11.3	0.893	14.3	0.827	15.2	0.931	10.0	0.877	9.8	0.816	13.7	0.850	11.3	0.893	14.3	0.827	15.2
Singh et al. (2023)[71]	0.928	7.15	0.890	7.6	0.834	10.2	0.868	9.6	0.902	10.6	0.852	11.7	0.928	7.15	0.890	7.6	0.834	10.2	0.868	9.6	0.902	10.6	0.852	11.7
Corral et al. (2021)[78]	0.927	11.2	0.877	9.7	0.815	14.0	0.852	11.1	0.892	13.6	0.834	15.0	0.927	11.2	0.877	9.7	0.815	14.0	0.852	11.1	0.892	13.6	0.834	15.0
Li et al. (2021)[79]	0.922	15.5	0.857	17.5	0.809	18.0	0.836	17.2	0.867	16.6	0.802	19.1	0.922	15.5	0.857	17.5	0.809	18.0	0.836	17.2	0.867	16.6	0.802	19.1
Khader et al. (2021)[80]	0.914	12.1	0.853	12.0	0.768	17.2	0.814	15.2	0.850	17.5	0.794	17.0	0.914	12.1	0.853	12.0	0.768	17.2	0.814	15.2	0.850	17.5	0.794	17.0
Carscadden et al. (2021)[81]	0.913	14.5	0.851	13.0	0.776	17.8	0.809	14.5	0.791	30.7	0.732	32.9	0.913	14.5	0.851	13.0	0.776	17.8	0.809	14.5	0.791	30.7	0.732	32.9
Scannell et al. (2021)[82]	0.905	13.6	0.848	15.5	0.772	17.2	0.820	17.5	0.876	16.2	0.809	19.6	0.905	13.6	0.848	15.5	0.772	17.2	0.820	17.5	0.876	16.2	0.809	19.6
Huang et al. (2021)[83]	0.896	15.7	0.772	23.0	0.761	17.9	0.721	20.2	0.820	21.0	0.698	29.5	0.896	15.7	0.772	23.0	0.761	17.9	0.721	20.2	0.820	21.0	0.698	29.5
Liu et al. (2021)[84]	0.889	16.0	0.835	14.2	0.785	22.1	0.808	18.9	0.814	22.1	0.758	22.0	0.889	16.0	0.835	14.2	0.785	22.1	0.808	18.9	0.814	22.1	0.758	22.0
Li et al. (2021)[85]	0.797	21.9	0.716	25.8	0.668	31.6	0.673	33.0	0.552	49.1	0.517	52.0	0.797	21.9	0.716	25.8	0.668	31.6	0.673	33.0	0.552	49.1	0.517	52.0
Singh et al. (2023)[24]	0.940	7.5	0.890	7.7	0.839	10.3	0.870	9.9	0.909	10.2	0.856	11.4	0.940	7.5	0.890	7.7	0.839	10.3	0.870	9.9	0.909	10.2	0.856	11.4
mnU (2D)	0.936	7.5	0.888	12.7	0.824	10.7	0.800	15.4	0.909	11.6	0.893	14.6	0.936	7.5	0.888	12.7	0.824	10.7	0.800	15.4	0.909	11.6	0.893	14.6
mnU (3D full resolution)	0.933	8.2	0.909	8.6	0.819	10.8	0.841	11.1	0.908	11.5	0.871	13.1	0.933	8.2	0.909	8.6	0.819	10.8	0.841	11.1	0.908	11.5	0.871	13.1
mnU (Ensemble)	0.937	7.4	0.888	8.5	0.826	9.9	0.864	9.9	0.913	10.8	0.852	12.7	0.937	7.4	0.888	8.5	0.826	9.9	0.864	9.9	0.913	10.8	0.852	12.7

Table A9: Performance comparison of nnU-Net variations and other models in MnM2 for Right Ventricle only. ShA- Short Axis, LoA - Long Axis, ED - End Diastole, ES- End Systole, DSC - Dice Score, HD - Hausdorff Distance.

Method	ShA						LoA					
	ED			ES			ED			ES		
	DSC	HD	DSC	DSC	HD	ES	DSC	HD	DSC	HD	DSC	HD
Fulton et al. (2021)[86]	0.934	9.610	0.910	10.032	6.227	0.935	10.032	6.227	0.935	6.227	0.904	5.935
Arega et al. (2021)[87]	0.932	10.078	0.910	9.782	6.028	0.935	9.782	6.028	0.935	6.028	0.905	6.188
Punithakumar et al. (2021)[88]	0.940	10.122	0.914	9.987	6.337	0.931	9.987	6.337	0.931	6.337	0.904	5.976
Li et al. (2021)[89]	0.933	10.563	0.907	10.050	6.246	0.930	10.050	6.246	0.930	6.246	0.902	6.097
Sun et al. (2022)[90]	0.937	10.879	0.913	9.874	6.056	0.935	9.874	6.056	0.935	6.056	0.904	6.031
Al et al. (2021)[91]	0.927	9.941	0.897	10.307	8.444	0.907	10.307	8.444	0.907	8.444	0.883	7.265
Liu et al. (2021)[92]	0.932	10.517	0.903	10.101	7.721	0.934	10.101	7.721	0.934	7.721	0.896	6.019
Jabbar et al. (2021)[93]	0.923	11.258	0.897	11.062	7.757	0.910	11.062	7.757	0.910	7.757	0.882	6.933
Queiros et al. (2021)[94]	0.924	11.327	0.898	11.447	7.173	0.922	11.447	7.173	0.922	7.173	0.900	6.391
Galati et al. (2021)[95]	0.916	11.681	0.890	11.747	7.840	0.924	11.747	7.840	0.924	7.840	0.894	6.978
Mazher et al. (2021)[96]	0.909	15.275	0.880	14.606	8.333	0.888	14.606	8.333	0.888	8.333	0.854	8.347
Gao et al. (2022)[97]	0.844	15.495	0.821	16.750	9.733	0.887	16.750	9.733	0.887	9.733	0.851	9.659
Beetz et al. (2021)[98]	0.873	16.682	0.820	17.913	8.570	0.896	17.913	8.570	0.896	8.570	0.864	7.591
Tautz et al. (2021)[99]	0.883	17.024	0.838	18.003	13.303	0.849	18.003	13.303	0.849	13.303	0.809	13.716
Galazis et al. (2021)[100]	0.852	19.430	0.821	19.117	18.629	0.814	19.117	18.629	0.814	18.629	0.781	17.198
nnU (2D)	0.934	10.50	0.934	11.228	-	-	11.228	-	-	-	-	-
nnU (3D full resolution)	0.934	10.393	0.934	10.301	6.055	0.934	10.301	6.055	0.934	6.055	0.900	6.108
nnU (Ensemble)	0.937	11.079	0.938	11.119	-	-	11.119	-	-	-	-	-